The Nançay H I Zone of Avoidance survey of 2MASS bright galaxies

Renée C. Kraan-Korteweg,[1][*] Wim van Driel,[2,3] Anja C. Schröder,[4]
Mpati Ramatsoku[1,5] and Patricia A. Henning[6]

[1]*Department of Astronomy, University of Cape Town, Private Bag X3, Rondebosch 7701, South Africa*
[2]*GEPI, Observatoire de Paris, PSL Research University, CNRS, Université Paris Diderot, 5 place Jules Janssen, F-92190 Meudon, France*
[3]*Station de Radioastronomie de Nançay, Observatoire de Paris, CNRS/INSU USR 704, Université d'Orléans OSUC, route de Souesmes, F-18330 Nançay,
France*
[4]*South African Astronomical Observatory, PO Box 9, Observatory 7935, Cape Town, South Africa*
[5]*INAF- Osservatorio Astronomico di Cagliari, Via della Scienza 5, I-09047 Selargius (CA), Italy*
[6]*Department of Physics and Astronomy, University of New Mexico, Albuquerque, NM 87131, USA*

ABSTRACT

To complement the Two Micron All Sky Survey (2MASS) Redshift Survey (2MRS) and the 2MASS Tully–Fisher survey (2MTF), a search for 21 cm H I line emission of 2MASS bright galaxy candidates has been pursued along the dust-obscured plane of the Milky Way with the 100 m Nançay Radio Telescope. For our sample selection, we adopted an isophotal extinction-corrected K_s-band magnitude limit of $K_s^o = 11\overset{m}{.}25$, corresponding to the first 2MRS data release and 2MTF, for which the 2MASX completeness level remains fairly constant deep into the Zone of Avoidance (ZoA). About one thousand galaxies without prior redshift measurement accessible from Nançay (Dec. $> -40°$) were observed to an rms noise level of $\sim$3 mJy for the velocity range -250 to $10\,600$ km s^{-1}. This resulted in 220 clear and 12 marginal detections of the target sample. Only few detections have redshifts above 8000 km s^{-1} due to recurring radio frequency interference. A further 29 detections and 6 marginals have their origin in non-target galaxies in the telescope beam. The newly detected galaxies are on average considerably more H I-rich (mostly 10^9–10^{10} M$_\odot$) compared to systematic (blind) H I surveys. The H I detections reveal various new filaments crossing the mostly uncharted northern ZoA (e.g. at $\ell \sim 90°$, $130°$, and $160°$), whilst consolidating galaxy agglomerations in Monoceros and Puppis ($\ell \sim 220°$ and $240°$). Considerably new insight has been gained about the extent of the Perseus–Pisces Supercluster through the confirmation of a ridge ($\ell \sim 160°$) encompassing the 3C 129 cluster that links Perseus–Pisces to Lynx, and the continuation of the second Perseus–Pisces arm ($\ell \sim 90°$) across the ZoA.

Key words: galaxies: distances and redshifts – galaxies: general – galaxies: ISM – radio lines: galaxies.

1 INTRODUCTION

Our understanding of the large-scale structures (LSS) and associated dynamics in the nearby Universe is increasingly being refined thanks to the advances of larger and more systematic redshift surveys (Jarrett 2004; Jones et al. 2009; Huchra et al. 2012; Tempel et al. 2014) and subsequent peculiar velocity surveys (Springob et al. 2014; Scrimgeour et al. 2016; Springob et al. 2016). Despite all these efforts, the overall bulk flow resulting from these studies can still not be fully reconciled with the dipole observed in the cosmic microwave background (Fixsen et al. 1996), nor is there

consensus about the volume which gives rise to the bulk flow (e.g. Hudson et al. 2004; Erdoğdu et al. 2006; Kocevski & Ebeling 2006; Carrick et al. 2015; Hoffman, Courtois & Tully 2015). This has left a gap in our knowledge of the local LSS and therefore considerable uncertainties in our understanding of the dynamics in the local Universe, cosmic flow fields and the dipole.

One of the major limitations remains the lack of data on galaxies in the so-called Zone of Avoidance (ZoA), caused by dust extinction and star crowding at low Galactic latitudes (see e.g. Kraan-Korteweg & Lahav 2000; Kraan-Korteweg 2005 for reviews). This zone is even wider in Galactic latitude for 'three-dimensional' (redshift) surveys, because optical redshifts are increasingly difficult to obtain for dust-obscured galaxies towards the Galactic plane.

[*] E-mail: kraan@ast.uct.ac.za

The ZoA is known to obscure and bisect major parts of dynamically important structures such as the Great Attractor (Dressler et al. 1987; Kraan-Korteweg et al. 1996; Radburn-Smith et al. 2006; Woudt et al. 2008; Staveley-Smith et al. 2016), the Perseus–Pisces Supercluster (PPS, Giovanelli & Haynes 1982; Focardi, Marano & Vettolani 1986; Hauschildt 1987) and the Local Void (Tully et al. 2008; Kraan-Korteweg et al. 2008). Moreover, the ZoA could still surprise us with completely unknown structures as postulated, for instance, by Loeb & Narayan (2008) – and which indeed are still being found, as demonstrated by the recently discovered Vela Supercluster (Kraan-Korteweg et al. 2015, 2017).

A vast improvement was achieved with the near-infrared (NIR) Two Micron All Sky Survey (2MASS; Skrutskie et al. 2006) from which an extended source catalogue of 1.6 million objects was extracted, (2MASX; Jarrett et al. 2003), which is uniform over the sky and much less affected by dust extinction than optical whole-sky surveys. It is complete to the magnitude limit of $K_s < 13\overset{m}{.}5$, and consists mostly are galaxies, apart from an increasing number of (extended) Galactic sources close to the Galactic Plane. Around the Galactic Bulge, 2MASX suffers some incompleteness though due to the high stellar density. According to Jarrett et al. (2000) galaxy counts start to drop where stellar density levels reach $\log N(\mathrm{SD}_{K_s<14\overset{m}{.}0}) = 3.6$ per sq deg, hence from about $-90° \lesssim \ell \lesssim +90°$ for latitudes below $|b| \lesssim 5°$. The Milky Way becomes completely opaque to galaxies where this level reaches $\log N = 4.5$, leading to a broadening of the NIR 2MASX-ZoA to $|b| \lesssim 8°$ for about $\Delta \ell \pm 30°$ around the Galactic Centre (GC). However, the Galactic Anticentre region ($90° < \ell < 270°$) – hence all of the northern ZoA – is not affected, at least not for the brightest 2MASX galaxies.

It is therefore not surprising that 2MASX was used as a basis for a systematic redshift follow-up, launched over a decade ago by John Huchra, to arrive at a homogeneous 'whole-sky' 2MASS Redshift Survey (2MRS) for LSS studies of the nearby Universe. Its release came in batches, starting in 2005 with the first online release (see e.g. Huchra et al. 2005), a survey of ∼23 000 galaxies which is complete to an extinction-corrected magnitude of $K^o \le 11\overset{m}{.}25$. The second data release goes half a magnitude deeper ($K^o \le 11\overset{m}{.}75$) and contains ∼44 500 galaxies (Huchra et al. 2012). Both versions however did not target 2MASX galaxies in the innermost ZoA ($|b| < 5°$; extending to $|b| < 8°$ around the Galactic Bulge) because of the inherent difficulties in getting good signal-to-noise (S/N) optical spectra for these heavily obscured galaxies.

This gap in the LSS maps of the nearby Universe has partly improved through systematic blind HI surveys, which do not suffer foreground extinction, e.g. HIPASS (the HI Parkes All-Sky Survey), at the 64 m Parkes radio telescope for the southern sky (Meyer et al. 2004; Koribalski et al. 2004), its northern extension to Dec. = +25° (Wong et al. 2006), and the ongoing HI 100 m Effelsberg radio telescope HI Survey (EBHIS) for the remaining northern sky (Kerp et al. 2011). But these surveys are shallow (rms ∼17–25 mJy), and sparsely sampled in comparison to optical and NIR whole-sky galaxy surveys in terms of detections per unit sky area (∼0.1 gal per sq deg) and the volume to which they are sensitive.

To improve on this situation a deeper HI survey (rms ∼6 mJy), focused specifically on the most opaque part of the ZoA ($|b| \le 5°$), was performed with the Parkes radio telescope: HIZoA encompasses the southern ZoA (Staveley-Smith et al. 2016) and its northern extension ($\Delta \ell = 16°$, Donley et al. 2005). But no similar systematic HI survey exists for the remainder of the northern ZoA, apart from selected regions pursued with the 305 m Arecibo telescope. These are the shallow ALFA ZoA survey (Henning et al. 2010) of the

inner Galaxy, at $|b| < 10°$ (rms ∼5 mJy), and the deep ALFA ZoA surveys (Henning et al. 2008) for both the inner and outer Galaxy ($|b| < 5°$, with an rms ∼1mJy).

This leads to a significant part of the northern ZoA that has not been surveyed in velocity space in any systematic way, in particular the ZoA range in between the declination strips accessible from Arecibo ($70° \lesssim \ell \lesssim 180°$). The latter is particularly relevant because it is home to the PPS, a dominant structure of the nearby Universe, which crosses the ZoA at two locations. The PPS has therefore never been fully charted. Another structure, the Supergalactic Plane crosses the GP in this part unexplored part of the ZoA as well, while other unknown structures may have gone completely unnoticed.

Following the success of our pilot study using the Nançay (NRT) and the Arecibo radio telescopes to survey 197 2MASS galaxy candidates in HI (van Driel et al. 2009), we decided in 2009 to fill in the 2MRS ZoA gap – in collaboration with the late John Huchra – and pursue a targeted HI survey of all the bright ZoA 2MASX galaxies that had no prior redshift information, and can be reached with the NRT, i.e. have declinations $\delta > -40°$. This implies a ZoA longitude range of $\Delta \ell = 280°$ covering $-20° \lesssim \ell \lesssim 260°$. To be compatible with 2MRS, our completeness limit was set $K_s^o < 11\overset{m}{.}25$ *after* corrections for foreground extinction (described in detail in Section 2). This limit corresponds to an optical *B*-band limit of $13\overset{m}{.}25$ for a typical spiral colour of $(B - K) \simeq 2\overset{m}{.}0$ (e.g. Jarrett et al. 2003), and is therewith comparable to the completeness limit of most optically selected nearby whole-sky surveys.

The resulting Nançay HI ZoA target list contains about one thousand 2MASX galaxies within the Galactic latitude range $|b| < 10°$, that had no prior redshift and were accessible from Nançay. Most are located within $|b| < 5°$. This paper focuses on the NRT HI observations pursued between 2009 – 2015, the resulting detection rates, galaxy properties, and a description of the new LSS uncovered by the Nançay HI-ZoA survey.

It should be noted that the results presented here form part of a much larger effort to (i) map the LSS across the full 360° circle of the ZoA, and (ii) to subsequently determine the peculiar velocity fields and underlying mass–density field for an adequately selected subsample of inclined spiral galaxies through an NIR Tully–Fisher (TF) analysis optimized for the ZoA (Said et al. 2015). The latter will complement the 2MASS Tully–Fisher Survey (2MTF; e.g. Masters, Springob & Huchra 2008; Hong et al. 2013, 2014; Springob et al. 2016; Howlett et al. 2017) which excludes the inner ZoA ($|b| > 5°$), since our data are based on a newly defined catalogue of 2MASS bright galaxies complete to the same extinction-corrected magnitude limit of $K_s^o \le 11\overset{m}{.}25$ for the whole ZOA within $|b| < 10°$ (2MZOAG; Schröder, van Driel & Kraan-Korteweg, in preparation, Paper I).

To achieve this, various other programs have been launched, that will be presented separately. These include an extension of the Nançay ZoA 2MASX target list to the more southern galaxies ($\delta < -40°$) using the Parkes radio telescope. HI observations of potential TF galaxies that have optical redshifts only, as well as of re-observations of HI detections whose S/N were too low to allow robust linewidth parametrization (Said et al. 2016b). The final step will be an application of the NIR TF relation optimized for the ZoA (see Said, Kraan-Korteweg & Jarrett 2015).

An independent approach towards a southern ZoA peculiar velocity analysis (Said et al., in preparation) consisted in a dedicated follow-up NIR imaging survey (Said et al. 2016a) of all the HI detections from the systematic (blind) HI survey HIZoA (Staveley-Smith et al. 2016), hence the other way around compared to starting

with a NIR selected sample. The two methods are complementary to each other in the sense that HIZoA has excellent coverage over the Galactic Bulge area where 2MASS galaxies are lacking, whereas the 2MASS bright galaxy sample is very complete over the remainder of the ZoA, ensuring coverage along the whole Galactic equator.

This paper is dedicated to reducing the 2MRS 'redshift ZoA' using the NRT and studying the newly unveiled LSS, in particular in the mostly unexplored region between $70° \lesssim \ell \lesssim 180°$. Its structure is as follows: the selection of the 2MASS ZoA galaxy candidates observed in H I is described in Section 2, the observations and data reduction procedures in Section 3, whilst the properties of the H I-detected and non-detected galaxies are detailed in Section 4. Section 5 follows with a description of the global properties of the NRT detections – a Hubble constant of $H_0 = 75$ km s^{-1} Mpc^{-1} was used for their derivation. The newly discovered LSS are discussed in detail in Section 6, ending with a summary in Section 7.

2 SAMPLE SELECTION

Our first 2MASX ZoA target list was provided in 2009 by John Huchra. It contained 2MASX galaxies within the Galactic latitude range $|b| < 10°$ that then had no prior redshift and were accessible with the NRT ($\delta > -40°$). It hence went wider than the 2MRS exclusion region: $|b| < 8°$ around the Galactic Bulge ($\ell < \pm 30°$) and $|b| < 5°$ elsewhere. The higher latitude range was motivated by the much lower fraction of completeness of the 2012 2MRS catalogue (Huchra et al. 2012) at the lowest latitudes ($\sim$17.8 per cent for 2MRS galaxies below $|b| < 10°$) compared to the overall superb completeness in redshift of the full catalogue of 97.6 per cent. And although the incompleteness fraction is significantly lower for the magnitude limit of the first data release ($K_s^o \leq 11\overset{m}{.}25$), that was not the case when we started out with this project in 2009. Moreover, the expectations were that radio observations at the 21 cm line might well have better success in capturing the redshifts of many of these optically obscured low-latitude 2MRS galaxies – at least for the ones containing gas.

The resulting Nançay observing list contained close to a thousand galaxies (for $K_s^o \leq 11\overset{m}{.}25$, $\delta > -40°$), excluding the roughly 350 2MASX ZoA galaxies in Huchra's private redshift catalogue, the so-called zcat, that he had compiled for latitudes below $|b| < 5°$.

During the course of our observing program it became clear that the original ZoA data set needed to be adjusted, particularly – but not exclusively – for the $|b| < 5°$ band. The reason was that we did encounter low-latitude 2MRS galaxies that were not in the original Huchra 2MRS target and ZoA lists. Moreover, we also found 2MASX objects that were not classified as galaxies, despite redshifts confirming their reality. As such it was decided to redefine the 2MASS galaxy ZoA list from scratch for the latitude range $|b| < 10°$ over the full band of the Milky Way.

The resulting 2MASS ZoA Galaxy catalogue (2MZOAG) is described in detail in a separate paper (Schröder, van Driel & Kraan-Korteweg, in preparation , Paper I) and forms the basis of all our further 2MASS ZoA studies, including a future analysis of the variation of the foreground extinction using the NIR colours of the ZoA galaxies themselves.

For the purpose of this paper, it suffices to say that the selection was based on the isophotal magnitude K_s-band magnitude, K_{20}, not the H band as for the 2MRS. We furthermore worked with isophotal magnitudes rather than total magnitudes because they are more robust when selecting galaxies that may have suffered some level of obscuration (Said et al. 2015). A further advantage of redefining

a low-latitude NIR galaxy catalogue was the availability of vastly increased multiwavelength sky-survey imaging data for the galaxy verification process, such as UKIDSS, VISTA, and *WISE*, in addition to the 2MASS J, H, K images, and the previously existing B, R, I images of the Digitized Sky Surveys. This made the identification process more secure. We furthermore took account of the foreground extinction $E(B - V)$ at the actual position of the source (Schlegel, Finkbeiner & Davis 1998), to ensure that all sources up to the *extinction-corrected isophotal* K_{20}-band magnitude limit of $K_s^o \leq 11\overset{m}{.}25$ entered the 2MZOAG. This did take into account the *additional* dimming due to the loss of the other low surface-brightness (SB) areas of a galaxy (Riad, Kraan-Korteweg & Woudt 2010) over and above the extinction A_K. This is relevant when trying to arrive at a complete NIR whole-sky survey that includes the ZoA. We added a few further galaxies to our target list that lie at higher latitudes. These are also located in high extinction regions, and were excluded in 2MRS and 2MTF because of their additional sample criterion of $E(B - V) < 1\overset{m}{.}0$.

In conclusion, our final Nançay target sample consists of 1003 galaxies at low Galactic latitudes. The distribution of all targets is displayed in Fig. 1; it shows the survey area in Galactic coordinates for the longitude range accessible with the NRT (given by the black curves). The green dots mark the 2MASX galaxies that have published redshifts, while the red and black dots indicate the target sample – red identifies the H I- detected galaxies and black the non-detections (see Section 4 for details). The displayed 2MASS galaxies are based on a combination of the 2MZOAG catalogue for $|b| < 10°$, and the 2MRS galaxies for $|b| \geq 10°$, both for $K_s^o \leq 11\overset{m}{.}25$.

To demonstrate the success in bridging the 2MASX bright galaxy distribution across the ZoA we present Fig. 2, which displays in the top panel a histogram of the distribution of the 2MZOAG catalogue as a function of Galactic latitude ($|b| < 10°$) for the Nançay survey declination range (see Paper I, for a description of the full 2MZOAG). Apart from fluctuations due to LSS, hardly any dip is notable in the galaxy counts at the lowest latitude, despite part of the Galactic Bulge area being included in the survey sample (see Fig. 1). The green histogram presents the 2MRS redshifts for $|b| > 5°$ – as published in Huchra et al. (2012) – with the addition of the low-latitude zcat compilation for $|b| < 5°$.

The difference between the black and green histograms formed the basis of our NRT target selection. The final and fully observed survey sample is given by the black histogram in the lower panel (as for Fig. 1, the H I detections are identified by the red histogram). Note, however, that the sum of the green histogram and the target sample do not entirely add up. During the course of the observations more redshifts became available, while a detailed literature search also revealed further published redshifts (2MZOAG; Schröder, van Driel & Kraan-Korteweg, in preparation).

3 OBSERVATIONS AND DATA REDUCTION

This section describes the actual NRT observing and data reduction procedures of the 1003 galaxy sample, followed in Section 4 by a presentation and analysis of the H I detections and non-detections. The NRT is a 100-m class radio telescope, with its 6900 m^2 collecting area. It is a meridian transit-type instrument, see e.g. van Driel et al. (2016) for further details on the instrument and data reduction. Due to the E-W elongated shape of the mirrors, some of its characteristics depend on the observed declination. Its half-power beam-width (HPBW) is 3.5 arcmin in right ascension, independent of declination, while in
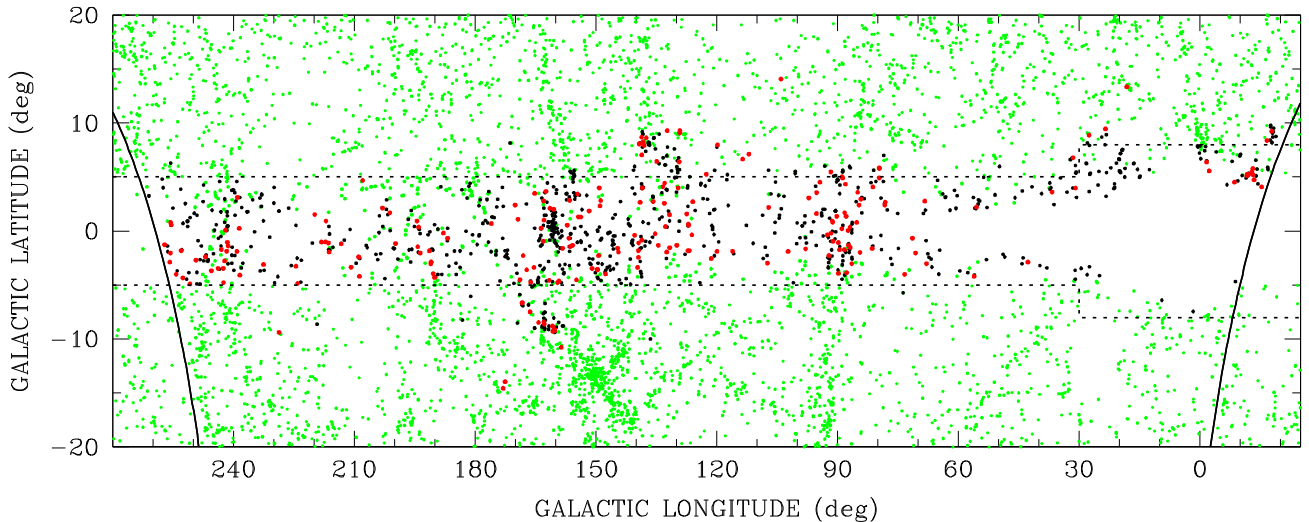
Figure 1. Distribution in Galactic coordinates of the 2MASX bright ($K° \leq 11^m25$) galaxy sample accessible with the NRT ($\delta > -40°$; black curves). The dotted black curve marks the nominal latitude limit of the 2MRS. Green dots mark galaxies with existing 2MRS and 2MZoA redshifts, the red and black dots our NRT target sample of galaxies without redshifts ($N = 1003$), of which 23 per cent were detected (red) with the NRT down to the survey sensitivity limit of rms = 3 mJy. The increasing 2MASS galaxy incompleteness in the inner ZoA towards the GC region due to star crowding is notable from $\ell < 80°$.
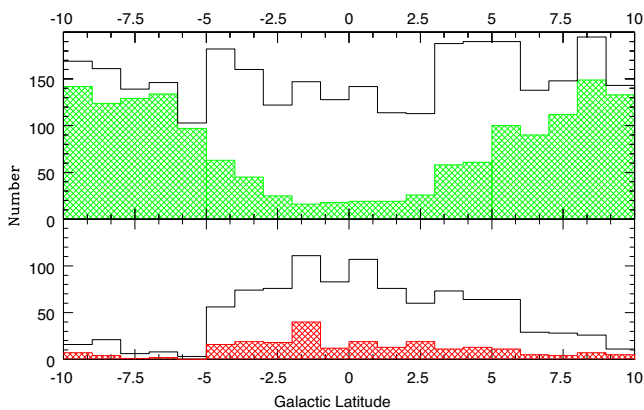
Figure 2. Histogram of the 2MASX ZoA bright galaxies with $|b| < 10°$ for the NRT visibility range $\delta > -40°$. Top panel: the black histograms demarcate all 2MZOAG galaxies and green are the ones with redshifts in 2MRS (Huchra et al. 2012) complemented by the low-latitude zcat compilation. Bottom panel: the Nançay target sample (all observed), where the red histogram highlights the H I detections (see Section 4).

declination it is 23 arcmin for $\delta < 20°$, rising to 32 arcmin at $\delta = 71°$ (see also Matthews & van Driel 2000). The instrument's sensitivity follows the same geometric effect and decreases correspondingly with declination. The typical minimum system temperature is 35 K.

Flux calibration is determined through regular measurements of a cold load calibrator and periodic monitoring of strong continuum sources by the Nançay staff. For verification and monitoring of the standard, regular NRT flux scale calibration of continuum sources, we also regularly observed H I line flux calibrator galaxies measured at Arecibo by O'Neil (2004). From the 51 NRT measurements, we derived a ratio between our total line fluxes and the literature values of 0.91 ± 0.08 (see van Driel et al. 2016 for details on the flux scale comparison). Note that we did not use these calibrator data to rescale the Nançay line fluxes presented in the next section.

We used an autocorrelator set-up of 4096 channels in a 50 MHz bandpass, with a channel spacing of $2.6\,\mathrm{km\,s^{-1}}$ and a velocity

coverage of -250 to $10\,600\,\mathrm{km\,s^{-1}}$ (or 1370–1421 MHz in frequency). The data were taken in position-switching mode, with an on-source integration time of 40 s per ON–OFF pair. The observations were made in the period of 2009 July–2015 December, using a total of about 1800 h of telescope time. Our aim was to keep integrating a source until an rms noise level of 3 mJy was reached, at a velocity resolution of $18\,\mathrm{km\,s^{-1}}$, unless a sufficiently high S/N profile was detected before the target rms value was reached.

We used standard NRT software to average the two receiver polarizations, perform the declination-dependent conversion from system temperature to flux density, fit polynomial baselines, smooth the data to a velocity resolution of $18\,\mathrm{km\,s^{-1}}$, and ultimately convert radial velocities to the optical, heliocentric system.

We also used standard NRT software to mitigate relatively strong radio frequency interference (RFI), see Monnier Ragaigne et al. (2003) for technical details. This allows us to identify unwanted time-variable RFI, and prevents mistaking it for genuine cosmic H I line signals. Removing such RFI but preserving underlying galaxian H I line signals is beyond the scope of the hard- and software used. The main sources of RFI are persistent, narrow terrestrial radars at velocities between ~ 8000 and $10\,000\,\mathrm{km\,s^{-1}}$, and a much broader, but intermittent, GPS signal centred on $\sim 8300\,\mathrm{km\,s^{-1}}$. The number of radars varies between observations but they are rarely all absent and in general so densely packed in velocity as to make the detection of galaxian H I lines in between them impossible. In the rare cases where the intermittent GPS signal is so strong that it causes baseline 'ringing' over a broad velocity range, the affected ON/OFF cycles are not used for further data analysis; otherwise the GPS signal is flagged but not removed.

Spectra of 34 sources appeared affected by a well-known instrumental baseline ripple (e.g. Wilson, Rohlfs & Huttemeister 2009) which can significantly increase the rms noise level. The ripple, related to the presence of a strong continuum source, is caused by reflected radiation in the telescope which forms a standing wave with a wavelength of about 115 $\mathrm{km\,s^{-1}}$. It is characterized by a narrow peak always at the same position in an Fast Fourier Transform (FFT) deconvolution of a spectrum, which can be effectively identified and removed; a second FFT transform then results in a

deripped line spectrum. This 'derippling' was performed by M.D. Lehnert, using a PYTHON routine written by him (see Butcher et al. 2016).

In our adjudication of detections, we divided them into four categories: clear, marginal, possible, and non-detections. This is based on independent visual inspections of the spectra as well as on the S/N parameter (cf. Saintonge 2007).

4 RESULTING DATA

With a total of 1013 pointings we observed 1003 2MASX galaxies above our extinction-corrected magnitude limit. This number includes 12 galaxies that lie in pockets of higher extinction of $E(B - V) \geq 1^{\mathrm{m}}0$ but lie above the $|b| > 10°$ survey border, and were therefore excluded from the original 2MRS (or TMF) samples. They are marked with the flag (e) in the tables discussed below.

Of the observed sample galaxies, 220 are clear and 10 marginal detections (four clear and one marginal lie above the ZoA). This constitutes a detection rate of 22 per cent, which is satisfactory given that (i) no pre-selection on type or likelihood of gas content was attempted, and (ii) the ZoA declination strips within reach of the Arecibo telescope had been covered extensively by Pantoja et al. (1997). These consisted of pointed H I observations of galaxies identified in a dedicated search on sky survey plates, hence many are NIR bright.

The 22 per cent detection rate is practically identical to the one obtained in our pilot project (van Driel et al. 2009) for the 2MASX galaxies observed with the NRT (not counting the deeper Arecibo targets), which reached similar rms levels.

A further 29 clear and 6 marginal detections were identified in the spectra which – after careful scrutiny – turned out to be the signal of another galaxy in the NRT beam. They are henceforth referred to as non-target detections and are listed in a separate table (Table 2). They have not been used in any of the subsequent analyses.

Nine galaxies that were not in our magnitude limited target list, but were observed *and* detected in the course of the program to confirm the H I flux of nearby sources and to avoid possible confusion issues with the actual target. Of these six were clearly deteced and three marginally. The tenth pointing of a non-sample galaxy confirmed the original sample galaxy detection. These 10 galaxies have not been used either in any of the subsequent analyses.

The remaining 773 galaxies were not detected (Section 4.3). This number includes 12 galaxies were a hint of a signal is seen. Despite increased integration times leading to rms values below our sensitivity limit, the S/N remained too low for a credible detection. We call these 'possibles', to differentiate them from the marginals whose signals, although weak, look realistic.

As has been shown in earlier systematic H I ZoA surveys (e.g. Henning 1997; Staveley-Smith et al. 2016), the H I detection rate is completely independent of the foreground extinction at which the 2MASX galaxies are located. This is substantiated with Fig. 3 which shows the detections as a fraction (per cent) of the total number of detections ($N = 230$; red histogram) versus the K-band foreground extinction A_K, together with the fraction over the total of the non-detections ($N = 773$; blue histogram). The two histograms are indistinguishable. Non-detections do not occupy higher extinction levels than detections.

Fig. 3 reveals furthermore that most of the observed 2MASX galaxies lie at intermediate extinction levels, i.e. 77.5 per cent lie at extinction levels below $A_K < 0^{\mathrm{m}}5$, while 90 per cent have extinctions less than $A_K = 0^{\mathrm{m}}7$ (i.e. $A_B \sim 7^{\mathrm{m}}8$). Only 3.5 per cent
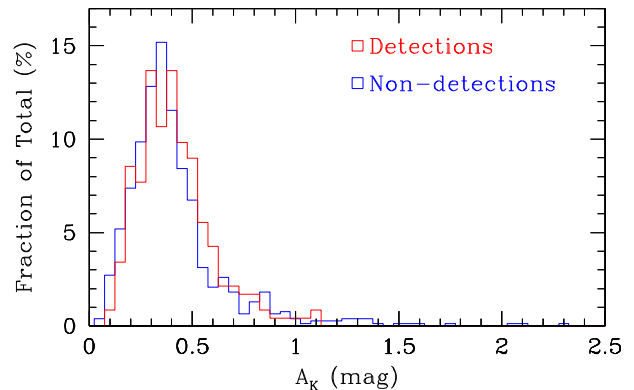
Figure 3. Distribution of extinction A_K of the in H I- detected galaxies (red; $N = 230$) versus the non-detections (blue; $N = 773$), both as a fraction of their respective total. As expected, the detection rate shows no dependence on foreground extinction.

of the bright 2MASX galaxy sample have higher extinctions than $A_K = 1^{\mathrm{m}}0$.

4.1 Detections

The observed H I parameters of the 220 clearly and 10 marginally detected target galaxies are listed in Table 1 as well as those of the nine detected non-sample galaxies together with their most relevant NIR photometric measurements (observed values, uncorrected for extinction). An extract of the first 10 galaxies is listed here. The complete table as well as all other tables are available online as Supporting Information.

The columns in the table are as follows:

Column 1: 2MASX J catalogue identifier for the J2000.0 coordinates used for the H I observations. In case the galaxy is not listed in the 2MASX catalogue (Tables A1c and 1d), the J2000 coordinates are given in brackets. Superscripts (flags) were appended to the name, where appropriate, to indicate the following:

– *a*: further notes on this galaxy are given in the Appendix available as online Supporting Information;

– *c* or *c?*: H I spectrum (possibly) confused by one or more additional galaxies in the telescope beam;

– *d*: derippled spectrum, that is, from which the effects of the baseline ripple were removed (see Section 3);

– *e*: the target forms part of the higher extinction sample, i.e. ($|b| > 10°$) (cf. Schröder, van Driel & Kraan-Korteweg, in preparation) and was observed for completeness; they are not used in the ZoA data analysis;

– *s*: the target is not in the original, magnitude limited, sample but was observed to check on the detection of another target (in case the galaxy is not listed in the 2MASX catalogue, their coordinates are given in bracktes);

– *v*: galaxy that has a published optical velocity inside the NRT search range;

– *v+*: galaxy with an optical velocity which lies outside the NRT search range.

Column 2: other name.

Column 3: the K_s-band magnitude measured within the r_{K20} isophotal aperture, K_{20}.

Columns 4 and 5: the ($J–K$) and ($H–K$) colours measured within the r_{K20} isophotal aperture.

Column 6: the elliptical aperture major axis at the 20 mag arcsec^{-2} K_s-band isophote, d_{K20} (in arcsec).
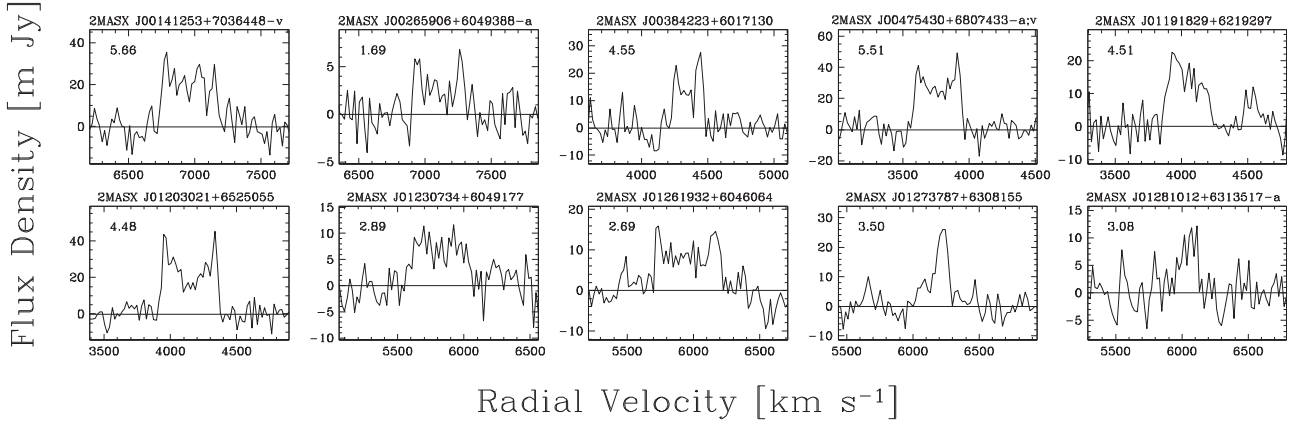
Figure 4. Example of the first two rows of the Nançay 21 cm H I line spectra of detected galaxies. The velocity resolution is $18\,\mathrm{km\,s^{-1}}$. The full figure of all detections (Tables 1 and 2 combined) is available online as Fig. A1.

Column 7: the minor-to-major axial ratio b/a, fit to the 3σ super-co-added isophote.

Columns 8 and 9: the heliocentric H I radial velocity determined as the centre of H I profile measured at the 50 per cent peak flux density, V_{50}, followed by its estimated uncertainty, σ_V (both in $\mathrm{km\,s^{-1}}$). The latter was determined following the formalism in Schneider et al. (1986, 1990),

$$\sigma_v = 1.5(W_{20} - W_{50})\mathrm{S/N}^{-1},$$

where W_{50} and W_{20} are defined below, and S/N is the signal-to-noise ratio (peak flux density divided by the rms).

Columns 10 and 11: the HI linewidths measured at 50 per cent and 20 per cent of the HI profile peak level W_{50} and W_{20}, respectively, uncorrected for galaxy inclination (in $\mathrm{km\,s^{-1}}$). Following Schneider et al., the uncertainty in the W_{50} and W_{20} linewidths is expected to be 2 and 3.1 times the uncertainty in V_{HI}, respectively.

Columns 12 and 13: the total measured HI line flux, F_{HI}, followed by its estimated uncertainty σ_F (in $\mathrm{Jy\,km\,s^{-1}}$),

$$\sigma_F = 2(1.2W_{20}R)^{0.5}\sigma,$$

where R is the instrumental resolution in $\mathrm{km\,s^{-1}}$ (see Section 3); also derived according to Schneider et al. (1986, 1990).

Column 14: the rms noise level values of the HI spectra (in mJy). The rms noise level was determined over a $3000\,\mathrm{km\,s^{-1}}$-wide part of the spectrum with low RFI occurrence. It is representative of the full velocity range as we have shown in a detailed analysis of about 50 spectra with little RFI and covering a wide range of observation time. There, we compared rms values in the velocity ranges 500–3500, 4000–7000, and 7000–$9000\,\mathrm{km\,s^{-1}}$ and found no differences within the errors.

Column 15: the S/N, determined by taking the linewidth into account, following the ALFALFA HI survey formulation from Saintonge (2007), i.e.

$$\mathrm{S/N} = 1000(F_{HI}/W_{50}) \cdot (W_{50}/2R)^{0.5},$$

where R is the instrumental resolution in $\mathrm{km\,s^{-1}}$ (see Section 3).

It should also be noted that the peak S/N (peak flux density divided by the rms) will be used in the text when discussing certain H I profiles. This parameter should not be confused with the ALFALFA linewidth-dependent S/N (Column 15 of Table 1). Furthermore, the observed and derived H I parameters of confused detections, contaminated by another galaxy in the telescope beam (indicated by the c flag in the tables) are uncertain. Likewise, the fluxes of galaxies observed at an offset to their centre position may be underestimated

(see the notes on individual galaxies in the Supporting Information for details).

The H I-line spectra of the detected galaxies are displayed as Supporting Information (Fig. A1) in order of right ascension. An example of the profiles of the 10 first listed in Table 1 is given in Fig. 4. In each of the panels, the identifying 2MASX name (Column 1) is given at the top, and the rms of the respective NRT observation in the top left corner. The profiles have been smoothed to a resolution of $18\,\mathrm{km\,s^{-1}}$. The full figure also contains the detections of non-target galaxies discussed below.

Detections of non-target galaxies: for completeness we list in Table 2, the cases where a galaxy other than the intended target was detected within the telescope beam – both certain and marginal detections. The table is arranged in a similar manner as Table 1 but without the NIR parameters. An extract of Table 2 is given on the preceding page; the full table is available online, their spectra incorporated in the electronic-only Fig. A1.

Column 1: 2MASX name of the targeted galaxy. Although an H I signal was identified, it has its origin in another galaxy. Where known the name of the source of the signal is given in the adjacent Column 2. One further flag was introduced (as superscript), in addition to the ones mentioned under the description of Table 1:

– *n*: the coordinates mark the target position, not of the source of the observed emission, which is offset from the pointing position;

Column 2: name of the galaxy from which the HI signal in the beam of the target originates (where identified).

Column 3: distance between the pointing position and the actually detected, non-target galaxy in the Nançay beam (in units of 0.5 HPBW).

Columns 4–11: The columns are identical to Columns $8-15$ in Table 1. All H I parameters are considered uncertain due to the off-beam detection.

4.2 Comparison with other redshift measurements

We started out with a target list of of bright 2MASX ZoA ($|b| < 10°$) galaxies without any prior redshift measurement in 2009. Since then, various redshifts for the original sample of 1003 galaxies have been observed. In addition, a renewed very careful literature search uncovered other measurements that had not been captured at the time the first target list was made available to us by Huchra. These are being used for a comparison here. We first discuss in-

Table 1. H I detections – observational data.

| 2MASX J | Other name | K_{20} | $J-K$ | $H-K$ | d_{K20} | b/a | V_{50} | σ_V | W_{50} | W_{20} | F_{HI} | σ_F | rms | S/N |
| | | mag | mag | mag | arcmin | | km s^{-1} | km s^{-1} | km s^{-1} | km s^{-1} | Jy km s^{-1} | Jy km s^{-1} | mJy | |
(1)	(2)	(3)	(4)	(5)	(6)	(7)	(8)	(9)	(10)	(11)	(12)	(13)	(14)	(15)
00141253+7036448[a,n,v]	PGC 2737274	10.92	1.37	0.39	53	0.70	6958	8	396	430	9.08	1.09	5.66	13.4
0038423+6017130[a,n]	ZOAG 121.35-02.54	10.94	1.20	0.31	51	0.74	4354	5	222	241	3.82	0.66	4.55	9.4
00475430+6807433[a,n,c,v]	ZOAG 122.61+05.26	10.86	1.42	0.50	74	0.30	3763	5	341	368	10.62	0.98	5.51	17.4
0191829+6219297[a,n]	ZOAG 126.16+00.37	10.67	1.67	0.52	62	0.22	4041	18	294	354	4.73	0.79	4.51	10.2
0203021+6525055	IRAS 01170+6509	9.96	1.43	0.45	80	0.54	4148	4	413	440	10.64	0.87	4.48	19.5
01261932+6046064	WEIN 013	10.15	1.43	0.48	64	0.60	5958	3	477	490	5.12	0.55	2.69	14.5
01273787+6308155	ZOAG 127.01+00.55	10.93	1.83	0.62	36	0.82	6223	40	95	294	3.65	0.56	3.50	17.8
0148559+6045514	IRAS 01455+6031	11.04	1.37	0.40	46	0.40	4391	11	266	311	5.73	0.77	4.70	12.5
01572719+6601408	IRAS 01536+6546	10.57	2.23	0.72	42	0.62	3905	17	224	292	2.62	0.48	3.03	9.6
02013241+6824219[a,v]	IRAS 01575+6809	9.59	1.37	0.41	89	0.88	3771	3	77	102	2.20	0.25	2.67	15.7

Table 2. H I detections of non-targets in the telescope beam.

| Target - 2MASX J | Detected object | Dist | V_{50} | σ_V | W_{50} | W_{20} | F_{HI} | σ_F | rms | S/N |
| | | 0.5 HPBW | km s^{-1} | km s^{-1} | km s^{-1} | km s^{-1} | Jy km s^{-1} | Jy km s^{-1} | mJy | |
(1)	(2)	(3)	(4)	(5)	(6)	(7)	(8)	(9)	(10)	(11)
01474890+6305128[a,n]	EZOA J0147+63	2.4	4243	16	189	248	1.74	0.36	2.44	8.7
02085980+7114029[a,n]	2MASX J02084091+7102087	1.1	3304	7	171	209	4.47	0.61	4.51	12.6
02531475+5528143[a,n,c,v]	Anon J025321.6+553602	1.3	3832	3	47	86	3.33	0.28	3.19	25.4
02531969+5529140[a,n]	Anon J025321.6+553602	1.0	3824	2	63	97	4.92	0.29	3.14	32.9
(0253216+553602)[s,a,n]	Anon J025321.6+553602	1.1	3826	5	60	113	4.26	0.41	4.13	22.2
03202205+6645055[a,n,v]	Anon J031958.7+664959	1.3	2993	3	175	197	4.20	0.36	2.78	19.0
03403139+6649043[a,n,v]	2MASX J03400768+6642470	1.4	1574	2	106	165	21.60	0.36	2.98	117.3
04114143+3841285[a,n,v]	2MASX J04113202+3846565	1.1	5698	20	102	191	1.34	0.24	1.87	11.8
04580945+3523013[a,n]	2MASX J04580771+3533503	0.9	6277	36	307	427	2.55	0.40	2.06	11.8
05583605+4031118[a,n,v]	2MASX J05583132+4031028	0.5	7661	36	207	330	3.03	0.65	3.87	9.1

dependent H I detections, followed by optical measurements in the Section 4.2.2.

4.2.1 Comparison to other H I detections

For 42 of the 220 detected galaxies we found a total of 75 H I measurements reported in the literature, many of these from the recent HIZoA survey (Staveley-Smith et al. 2016). Their H I parameters are given in Table 3 together with the NRT parameters (the first 10 lines are listed; the full table is available online). The entries in the table are:

Columns $1 - 5$: provide the 2MASX name and main NRT H I-parameters V_{50}, W_{50}, W_{20}, and F_{HI} as listed in Table 1.

Columns $6 - 9$: gives the same H I parameters as reported in the literature.

Column 10: gives the telescope code: 91m = NRAO 91 m, ARE = Arecibo 305 m, EFF = Effelsberg 100 m, GBT = Green Bank Telescope, JBO = Jodrell Bank 76 m, NRT = Nançay 94 m equiv., PKS = Parkes 64 m, and VLA = Very Large Array 27 × 2 5m.

Column 11: the reference code Ref. refers to the paper which published the literature values. The references are given at the end of the table.

For the following analysis, we exclude the reported detection of 2MASX J05014040+4338109 by Hauschildt (1987) because its H I flux of 1.3 ± 0.9 Jy km s^{-1} is very uncertain. The spectrum shows a baseline ripple and the velocity of 5161 km s^{-1} agrees neither with the NRT measurement of 7194 km s^{-1} nor with two other measurements of this galaxy. Fig. 5 presents the comparison of the central H I velocities, W_{50} linewidths and total line fluxes. Six (probably) confused cases are marked with a cross and excluded from the analysis.

The central H I velocities agree well, the mean difference and its standard deviation between our measurements and the literature values is (−0.3 ± 1.5) and 1417 km s^{-1}, respectively.

The W_{50} linewidths also agree well: they have a mean offset of (−3.7 ± 1.6) km s^{-1} and a standard deviation of 12.1 km s^{-1}. The six outliers (and likely confused cases) are

– 2MASX J03480963+4955140: 233 versus 351 km s^{-1}, observed with the NRT,
– 2MASX J04120068+3846073: 491 versus 591 km s^{-1}, observed with the GBT,
– 2MASX J05014040+4338109: 506 versus 579 km s^{-1}, observed with the 91m at Green Bank,
– 2MASX J05221454+3826469: 340 versus 626 km s^{-1}, observed with the GBT,
– 2MASX J06225815+1108312: 359 versus 252 km s^{-1}, observed with Arecibo,
– 2MASX J16463421−3903086: 224 versus 138 km s^{-1}, observed with Parkes.

Although their W_{50} values are quite different, the W_{20} widths for 2MASX J06225815+1108312 and 2MASX J16463421−3903086 are comparable (239 versus 260 and 395 versus 336 km s^{-1}, respectively). 2MASX J05014040+4338109 has no 91 m W_{20} width measurement as is the case for the two GBT detections. We find that 2MASX J16463421−3903086 is confused in the Parkes beam, but is fine in our observation; 2MASXJ05014040+4338109 has a second 91 m measurement which agrees well with our observation, and 2MASX J06225815+1108312 was also observed with Parkes and this agrees well with the NRT measurement. 2MASX J03480963+4955140 was also observed with the NRT which suffers heavily from RFI above $v = 8000$ km s^{-1}; this could easily affect either of the the linewidth measurements. The difference in central velocity is acceptable though at 23 km s^{-1}.

The literature H I line fluxes are on average 1.41 ± 0.04 times higher than the NRT values (excluding the NRT confused target and non-target detections). A detailed comparison of H I line fluxes measured recently at the NRT and at other telescopes (for both pointed and blind surveys) is presented in van Driel et al. (2016) for the Nançay Interstellar Baryons Legacy Extragalactic Survey (NIBLES; see their table A4). The NRT flux scale is consistent (0.91 ± 0.08 here, 0.88 ± 0.09 for NIBLES) with the single-horn Arecibo measurements of O'Neil (2004). More than half (35/60) of the ZoA literature values we used for our flux scale comparison are from the Parkes HIPASS and HIZOA multibeam surveys, for which we find a mean ratio of 1.44 ± 0.04, which is consistent with the 1.34 ± 0.28 found for NIBLES.

The H I flux scale comparison in van Driel et al. (2016) focused on the differences between single beam pointed observations and total fluxes reconstituted from data cubes obtained for blind surveys, such as HIPASS at Parkes and ALFALFA at Arecibo. For the ALFALFA α.40 catalogue (Haynes et al. 2011), a mean ALFALFA/NRT flux scale ratio of 1.45 ± 0.17 was found, similar to the HIPASS/NRT ratios mentioned above. Exploratory tests were made for NIBLES using an Arecibo multi-beam receiver data cube obtained for AGES, the Arecibo Galaxy Environment Survey (Minchin et al. 2010). These indicated that even for point sources changing the way in which total line fluxes are reconstructed can significantly change the result (see van Driel et al. 2016). A full analysis is beyond the scope of NIBLES and the present work.

4.2.2 Optical versus NRT redshifts

For 168 galaxies, we have found 170 optical redshifts. We have compiled their values in Table 4, ordered by RA (again only the first 10 lines are listed; the full table can be found online). The columns provide the following information:

Column 1: 2MASX identifier of the targeted galaxy. A further superscript *r* was introduced to mark the galaxies with an optical velocity that fall in the velocity range affected by radar RFI (8500−10 000 km s^{-1}).

Column 2: the star under Δv-flag indicates whether the optical velocity differs from the V_{50} NRT values by more than three times the uncertainty in the optical velocity or by more than 150 km s^{-1} where no uncertainty was published.

Columns 3 and 4: the heliocentric radial velocity measured in the optical V_{opt} and its estimated uncertainty, σ_v, (in km s^{-1}).

Column 5: the 'Ref.' codes are detailed at the end of the table.

For 11 detected objects the difference between the H I velocity and the optical velocity is larger than three times the uncertainty in the optical velocity, σ_v, whereas for four others without a published uncertainty it exceeds 150 km s^{-1}. Most (11/15) of these cases concern non-confused H I detections. For eight of these, the velocity differences are quite significant, i.e. either more than ∼5σ_v (2MASX J00475430+6807433, J02013241+6824219, J03292042+6601389, J04534877+4220445, J07483070−2532370, and J16490239-3642570), or more than 300 km s^{-1} otherwise (J07403156-−2618279 and J22540054+6728086); see also the notes in the Supporting Information.

Non-target detections: of the clear and marginal non-target detections, seven and two (28 per cent and 33 per cent) have published optical velocities. Not surprisingly, the majority (four and two, re-

Table 3. Comparison with literature H I detections.

2MASX J	V_{50}	W_{50}	W_{20}	F_{HI}	V_{50}	W_{50}	W_{20}	F_{HI}	Tel	Ref.
			— Nançay —				— Literature —			
	km s^{-1}	km s^{-1}	km s^{-1}	Jy km s^{-1}	km s^{-1}	km s^{-1}	km s^{-1}	Jy km s^{-1}		
(1)	(2)	(3)	(4)	(5)	(6)	(7)	(8)	(9)	(10)	(11)
00384223+6017130	4354	222	241	3.82	4355	219	228	$*$	VLA	H92
01191829+6219297	4041	294	354	4.73	4050	306	316	7.05	NRT	P03
02550583+6624065^v	3487	381	427	6.76	3456	374	390	12.31	JBO	L03
(0319587+664959)^{s,a}	2995	175	195	11.28	3005	185	200	16.03	JBO	L03
03290640+6458319^v	2464	416	446	10.53	2456	411	453	13.18	JBO	L03
03292042+6601389^{a,v}	2113	349	372	4.17	2111	358	379	4.33	GBT	M14
03480963+4955140^{a,c,v}	9991	233	453	4.19	9968	351	366	2.37	NRT	P03
04075531+4549400	4470	276	310	11.88	4470	287	320	11.48	NRT	P03

Notes. References:
C99: Chamaraux et al. (1999), C09: Courtois et al. (2009), D05: Doyle et al. (2005), H87: Hauschildt (1987), H88: Haynes et al. (1988), H92: Henning (1992), H00: Henning et al. (2000), H10: Henning et al. (2010), H86: Huchtmeier & Richter (1986), K87: Kerr & Henning (1987), K92: Kraan-Korteweg & Huchtmeier (1992), K04: Koribalski et al. (2004), L90: Lu et al. (1990), L03: Lang et al. (2003), M90: Martin et al. (1990), M04: Meyer et al. (2004), M14: Masters et al. (2014), P97: Pantoja et al. (1997), P03: Paturel et al. (2003), R00: Rosenberg & Schneider (2000), R02: Ryan-Weber et al. (2002), S94: Seeberger, Huchtmeier & Weinberger (1994), S05: Springob et al. (2005), S16: Staveley-Smith et al. (2016), and W06: Wong et al. (2006).

spectively) have significantly different H I velocities compared to the actual 2MASX target.

4.3 Non-detections

As described earlier, the majority of the targeted galaxies were not detected in the 21 cm line. We present their positions, NIR parameters – both observed and extinction-corrected – as well as the rms of the NRT H I observation. The columns are a mixture of observed (as defined in Table 1) and extinction-corrected properties. The first 10 galaxies are listed in Table 5, the full complement is available online.

Columns 1 and 2: 2MASX identifier and an alternate name (as in Table 1).

Columns 3 and 4: Galactic coordinates (Columnd 3 and 4).

Column 5: K_{20}-band magnitude measured at the r_{K20} aperture (as in Table 1).

Column 6: Galactic foreground extinction in the K_s band, estimated from the Schlegel et al. (1998) DIRBE (Diffuse Infrared Background Experiment)/*IRAS* extinction values $E(B-V)$ at the position of the source (henceforth SFD98). We correct the SFD98 *EBV* values for the factor of $f = 0.86$ derived in Schlafly & Finkbeiner (2011). Following Fitzpatrick (1999), a conversion factor of $R_K = 0.373$ was applied to arrive at the A_K-value.

Column 7: extinction-corrected isophotal K_s-band magnitude, $K_s^{o,d}$. The extinction correction follows the precepts of Riad (2010), i.e. the magnitude is not only corrected for the global foreground extinction at the position of the galaxy, A_K, but includes an additional correction to substitute for the loss of the low SB features that have fallen below the 20th isophote because of the reduction in SB at each pixel of the galaxy's extent. Such a loss is not fully recovered when extrapolating towards magnitudes as has been shown conclusively in Said et al. (2015, see their fig. 1). We therefore prefer isophotal over total magnitudes when working in areas of extinction, or with low SB objects. We added the superscript d (for diameter, respectively areal loss) to the standard superscript o to emphasize this additional correction term to the standard A_K correction.

Columns 9 and 10: extinction-corrected colours $(J - K)^\circ$, $(H - K)^\circ$ at the fixed r_{K20} isophote, hence corrected by $(A_J - A_K)$ and $(A_H - A_K)$ at said radius. Size corrections are superfluous for

isophotal colours as long as the radius at which they are determined is fixed.

Column 11: the rms of the observation. The rms noise level was determined over a 3000 km s^{-1}-wide part of the spectrum with low RFI occurrence (as described in Table 1).

The distribution of the rms noise levels of all the NRT non-detections are displayed in Fig. 6. The mean rms noise level of our non-detections is 2.5 mJy. This would imply a 3σ detection limit of $\log(M_{HI}) = 9.4$ M$_\odot$, for a flat-topped profile with a W_{50} of 300 km s^{-1} at a velocity of 5000 km s^{-1}, the mean values for our detections, hence nearly half a magnitude below the characteristic H I-mass M_{HI}^* (e.g. Zwaan et al. 2003; Martin et al. 2010).

Possible detections: for 12 of the non-detection pointings, a tentative detection could be identified. None of these tentative detections has a published velocity to ascertain their reality. They do require higher sensitivity for confirmation. To not lose the information, nor confuse them with detections and marginals, these possible but unconfirmed detections are listed in a separate table (Table 6) with their approximate H I parameters. The columns are identical to Table 5.

4.3.1 Optical redshifts of non-detections

Of the non-detections, 117 have published optical velocities, two of which with more than one determination. These are included in Table 4 for information. In the following, we use these measurements to assess whether we would have expected to detect this galaxy in H I.

In 24 cases, the optical velocity lies outside the NRT search range; their 2MASX names have been flagged with a '$v+$'. Note however, that 2MASX J16490239−3642570 with $V_{opt} = 30\,028$ km s^{-1} was clearly detected by us at $V_{HI} = 6385$ km s^{-1} (Table 1).

A further 12 sources with published optical or H I velocities in the range 8500−10 000 km s^{-1} are covered by radar RFI, which renders their detection nearly impossible. They have been added to Tables 1, 3 and 4, but with the flag 'r'. Despite the recurring RFI, we did detect seven galaxies in this RFI-plagued velocity range (Table 5).

Four of our non-detections have H I detections reported in the literature (added at the end of Table 3):
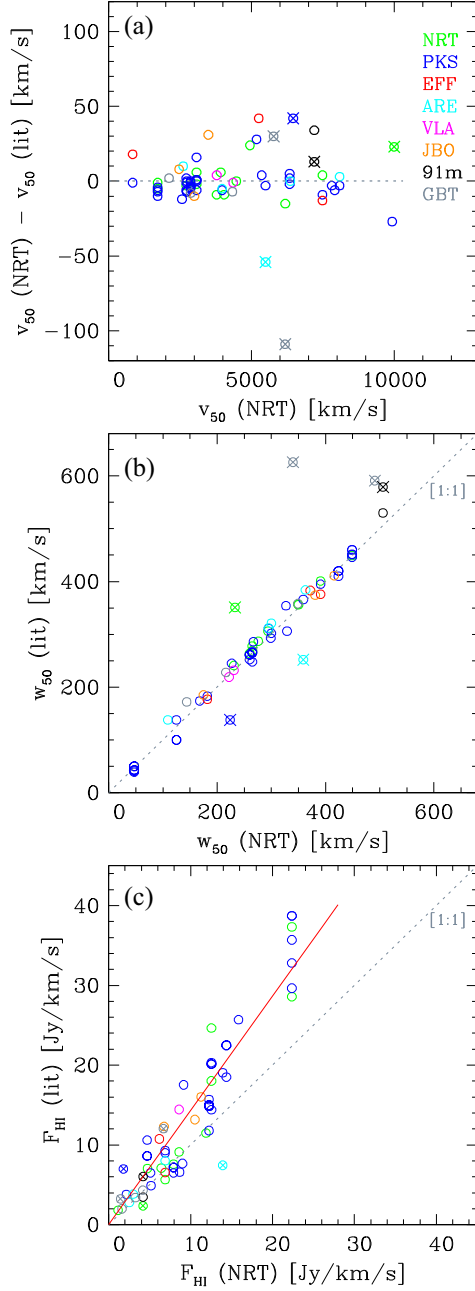
Figure 5. NRT versus literature H I line profile parameters. The colours identify the telescope used, the crosses (probably) confused profiles, the dashed lines equality, the red line (bottom panel) the slope (1.43) of a fit. Top panel: difference between the central line velocities as function of the NRT value. Middle panel: NRT W_{50} values versus literature. Bottom panel: NRT H I line fluxes versus literature.

– 2MASX J02121002+6144326 (V_{HI} = 5900 km s^{-1}, Kerr & Henning 1987),

– 2MASX J07003437−1020151 (V_{HI} = 9608 km s^{-1}, Staveley-Smith et al. 2016),

– 2MASX J20401346+5059165 (V_{HI} = 2783 km s^{-1} and V_{opt} = 3028 km s^{-1}, Paturel et al. 2003; Huchra et al. 2012),

– 2MASX J22131198+6153077 (V_{HI} = 3839 km s^{-1}, Seeberger et al. 1994).

It is not surprising that we did not confirm these detections. The first one has a positional uncertainty of 5−10 arcmin which means it

Table 4. Optical velocities in the literature.

2MASX J	Δv-flag	$V_{\rm opt}$ km s^{-1}	σ_v km s^{-1}	Ref.
(1)	(2)	(3)	(4)	(5)
00141253+7036448		6973	43	H12
00253292+6821442		3598		M08
		3729	54	H12
00475430+6807433^a	∗	1273	65	H12
01311294+6735115		10345	46	H12
01474890+6305128^a		4211	58	H12
01582742+6744421^{v+}		31270	44	H12
02013241+6824219^a	∗	4554	55	F95
02021798+6721240		3762	25	H12
02034762+6843532^r		9321	18	H12

Notes. References:
B09: Beckmann et al. (2009), C08: Crook et al. (2008), D90: Djorgovski et al. (1990), D91: Dressler (1991), F95: Fisher et al. (1995), G08: Goncalves et al. (2008), H12: Huchra et al. (2012), H91: Hewitt & Burbidge (1991), H95: Huchra, Geller & Corwin (1995), J09: Jones et al. (2009), K11: Koss et al. (2011), L99: Lawrence et al. (1999), M96: Marzke, Huchra & Geller (1996), M98: Motch et al. (1998), N97: Nakanishi et al. (1997), P09: Parisi et al. (2009), R11: Ricci et al. (2011), S85: Spinrad et al. (1985), S92: Strauss et al. (1992), S98: Seeberger & Saurer (1998), S00: Saunders et al. (2000), T94: Takata et al. (1994), V96: Visvanathan & Yamada (1996), Y93: Yamada et al. (1993), and Y94: Yamada et al. (1994).

could be a hidden galaxy outside of our NRT beam; its reported line flux could not be reduced to a value in Jy km s^{-1} (see Supporting Information). The second one is covered by radar RFI at the NRT and the third is a very weak detection (the reported peak S/N would be only 1.6× rms). For the fourth galaxy, the reported peak S/N and its uncertainty corresponds to 4.7 ± 1.3 × rms noise level – this marginal-looking detection we could, however, not confirm.

5 OBSERVED AND GLOBAL PROPERTIES OF THE DETECTED GALAXIES

When discussing and interpreting the parameter space of the newly obtained NRT H I data, caution is advised. This second paper of our bright 2MASX ZoA galaxy series is aimed at completing – as best as possible – the existing redshift gap in the zone of obscuration using the 21 cm line emission of neutral gas which is not affected by dust obscuration. The observed sample therefore does *not* constitute a complete sample, despite the imposed NIR magnitude completeness limit, because only galaxies which at the start of our observing campaign had no prior redshift were targeted (see Section 2). Of course, the large fraction of non-detections also play a role, but that is a bias we have in common with all targeted H I observations of galaxies. Our sample is close to a targeted magnitude complete sample for the inner ZoA ($|b| < 5°$), for which only a small fraction had published redshifts.

5.1 Observed H I parameters

In Fig. 7, we present histograms of the H I-parameters of the detected galaxies including the 10 marginals. The different panels represent the velocity distribution, V_{50}, the linewidth measured at the 50 per cent level, W_{50}, and the rms of the detected galaxies, and will be discussed in this order.

The velocity distribution in the top panel is mostly representative of the inner ZoA ($|b| < 5°$), since 180 out of the 230 detections (78 per cent) lie within that latitude range. A further 44 galaxies

Table 5. H I non-detections – observational data.

| 2MASX J | Other name | l | b | K_{20} | A_K | $K_s^{o,d}$ | $(J - K_s)^{o,d}$ | $(H - K_s)^{o,d}$ | rms |
| | | deg | deg | mag | mag | mag | mag | mag | mJy |
(1)	(2)	(3)	(4)	(5)	(6)	(7)	(8)	(9)	(10)
00161976+7025219	∗	119.97	7.75	11.33	0.32	10.95	0.54	0.17	3.54
00223972+6139447	∗	119.52	− 1.02	11.49	0.54	10.77	0.89	0.23	2.84
00253292+6821442^v	ZOAG G120.54+05.61	120.54	5.61	10.05	0.32	9.67	0.92	0.25	3.31
00281959+6447011	∗	120.47	2.02	11.84	1.01	10.52	0.51	0.16	3.52
00303425+6444585^d	∗	120.71	1.97	11.82	0.54	11.14	1.05	0.24	2.31
00314802+6227440	∗	120.66	− 0.32	11.88	0.61	11.08	∗	∗	3.07
00321813+6029565	ZOAG G120.58−02.29	120.58	− 2.29	11.38	0.25	11.09	0.92	0.23	2.53
00343086+6257451	ZOAG G121.01+00.15	121.01	0.15	11.23	0.45	10.67	0.65	0.12	2.11
00343656+6310260	∗	121.04	0.36	11.53	0.47	10.95	0.91	0.19	2.93
00360888+6319171	∗	121.22	0.50	11.37	0.42	10.86	1.36	0.49	2.20
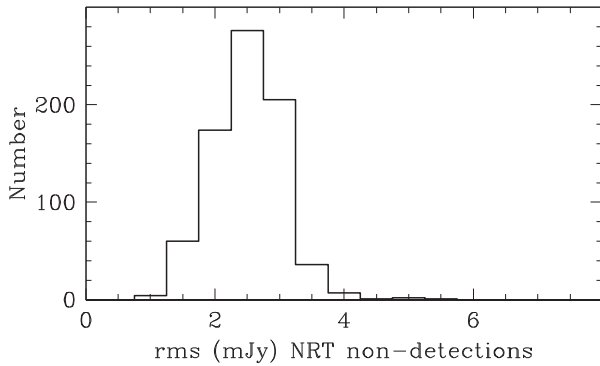
Figure 6. Distribution of the rms noise levels of the 771 H I non-detections. Apart from a few exceptions our nominal completeness limit of 3.3 mJy was reached throughout.

(20 per cent) were found in the latitude strips $5° < |b| < 10°$ (see also Fig. 1). The other 5 detections (2 per cent) were made at higher latitude in the high-extinction pockets.

Galaxies are found over most of the observed redshift range, with the majority lying within 2000–8000 km s^{-1}. The rather strong fall-off for $V \gtrsim 8000$ km s^{-1} is mostly due to recurring radar RFI around 8500 km s^{-1}, particularly notable in Fig. 8, in addition to the loss of sensitivity given our rms limit of 3 mJy. The counts pick up again around 10 000 km s^{-1} where we find four high H I-mass detections. Although not quite as persistent, RFI may have affected the detection rate around ∼3500 km s^{-1}.

The velocity histogram shows two clear peaks over and above what is expected from a more homogeneous galaxy distribution, a minor peak around 4000 km s^{-1} and quite a prominent one with broad shoulders at 6000 km s^{-1}. As will be seen in the LSS section, both of these peaks are associated with the PPS through two different entry points into the ZoA, as well as a completely new and unsuspected filament/wall-like structure in between those two.

The linewidth distribution (second panel) has quite an interesting shape in the sense that its distribution is nearly flat between linewidth of $150 < W_{50} < 400$ km s^{-1}, with few narrow and also broad linewidths spirals. The latter is more standard. This is very different to either systematic 'blind' H I surveys or targeted H I follow-up surveys. For instance, the linewidth distribution of the HIZoA (Staveley-Smith et al. 2016) with an rms of 6 mJy finds the large majority of detections between W_{50} of $50 − 200$ km s^{-1}, followed by a rapid decline for increasing linewidth above 200 km s^{-1} (see their fig. 2). The NRT detection sample is probably more di-

rectly comparable to the Parkes H I observations of optical ZoA galaxies pursued by Kraan-Korteweg, Henning & Schröder (2002) and Schröder, Kraan-Korteweg & Henning (2009) which has a similar rms limit and also primarily targeted galaxies without prior redshift measurement. Although not presented in these papers, the W_{50} distributions are not flat, however, but rather Gaussian in shape with a peak around 220 km s^{-1} followed by a slow decline towards the higher values. While the underrepresentation of very low linewidth galaxies in our NRT sample can partly be explained by the NIR selection which inherently biases against blueish, low SB gas-rich dwarfs, it does not explain the overall flatness of the W_{50} distribution.

The last panel shows the rms of the detections. The mean is a bit higher than that of the non-detections, 2.78 versus 2.50 mJy (Fig. 6), while its dispersion is broader (0.96 VERSUS 0.54 mJy). It has a higher number of detections with lower rms values ($\lesssim 3$ mJy) which is due to the extra integration that was added to firm up weaker detections. There also is a higher number towards larger rms values. This is due to our survey strategy of starting with shorter integrations to capture high S/N profiles early on, and not waste integration time.

5.2 Global properties

In Table 7, the global parameters of the 230 HI-detected galaxies, including NIR properties such as extinction-corrected magnitudes and colours, and HI mass-to-light ratios are listed. All global properties are based on a Hubble constant of $H_0 = 75$ km s^{-1} Mpc^{-1}. The 10 marginal detections of targeted 2MASX ZoA galaxies are added at the bottom of the table. The full table is online, the first 10 galaxies are shown in the sample table presented here. The explanation of the columns are:

Column 1: same as column 1 in Table 1.

*Columns 2 and 3:* Galactic longitude and latitude, ℓ and b, of the target galaxy.

Column 4: Galactic foreground extinction A_K estimated from the Schlegel et al. (1998, SFD98) DIRBE/*IRAS* extinction values $E(B − V)$ at the position of the source (see Table 5 for further details).

Column 5: distance $D = V_{LG}/H_0$, where the target's radial velocity (in km s^{-1}) with respect to the Local Group was adopted as $V_{LG} = V_{HI} + 300 \sin l \cos b$, with a Hubble constant of $H_0 = 75$ km s^{-1} Mpc^{-1}.

Column 6: extinction-corrected isophotal K_s-band magnitude, $K_s^{o,d}$ measured at the $r_{K_s}^{o,d}$ aperture. The extinction correction follows the precepts of Riad (2010).

Table 6. Possible H I detections – observational data.

2MASX J	Other name	K_{20}	$J-K$	$H-K$	d_{K20}	b/a	V_{50}	σ_V	W_{50}	W_{20}	F_{HI}	σ_F	rms	S/N
		mag	mag	mag	arcsec		km s^{-1}	km s^{-1}	km s^{-1}	km s^{-1}	Jy km s^{-1}	Jy km s^{-1}	mJy	
(1)	(2)	(3)	(4)	(5)	(6)	(7)	(8)	(9)	(10)	(11)	(12)	(13)	(14)	(15)
02590152+5318199	ZOAG G141.41−04.92	11.49	1.35	0.38	38	0.32	7146	8	229	250	0.79	0.30	2.05	4.3
03104409+6106477[a]	ZOAG G138.96+02.65	8.08	1.51	0.48	133	0.54	2505	38	162	267	1.47	0.41	2.73	7.1
03192996+5755423	*	11.61	1.39	0.48	24	0.78	1327	15	254	291	1.55	0.41	2.58	6.3
04110830+3837269B	*	10.90	1.45	0.45	46	0.34	6158	13	234	273	1.62	0.31	2.03	8.7
04264449+3810182	2MFGC 03603	10.87	2.07	0.65	61	0.30	6546	32	129	216	0.82	0.24	1.77	6.8
04292626+4855120	ZOAG G155.28+00.24	10.87	1.62	0.53	45	0.42	7231	30	94	154	0.55	0.25	2.18	4.3
04413675+4203562	*	11.13	1.44	0.38	38	0.48	3975	22	99	147	0.36	0.14	1.27	4.7
05141860+4622066	ZOAG G162.04+04.44	10.73	1.25	0.31	61	0.46	6388	8	388	405	1.21	0.36	1.90	5.4
06162583+1654326	*	11.59	1.60	0.53	38	0.60	5131	54	55	239	1.18	0.33	2.30	11.5
18202335−0117447	2MFGC 14346	11.47	1.69	0.51	53	0.20	6875	11	455	484	1.63	0.44	2.14	6.0
20135618+4443093[v]	2MIG 2761	11.29	1.52	0.50	45	0.42	7078	9	360	383	1.69	0.40	2.22	6.7
21071353+456529[c?]	*	10.34	1.58	0.45	50	0.90	4793	28	460	535	3.13	0.59	2.75	8.8
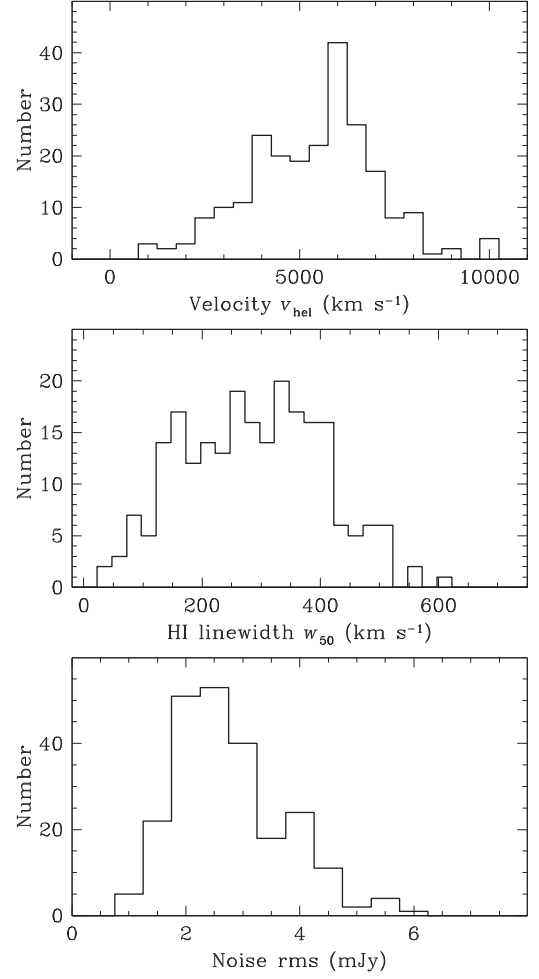
Figure 7. H I parameters of the detected galaxies ($N = 230$) and include, from top to bottom: the heliocentric velocity, the W_{50} linewidth, and the rms noise histograms. All panels include the 10 marginal detections (Table A1).
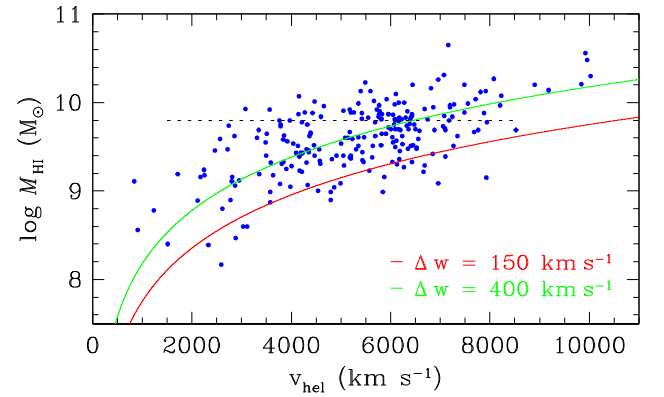
Figure 8. H I mass versus velocity plot for the 230 detected galaxies. The two displayed 3σ sensitivity curves represent linewidths of tex111 $\Delta W_{50} =$ 150 and 400 km s^{-1}, the range covered by the majority of our detections (see panel 2 in Fig. 8). The dashed black line is indicative of log M_{HI}^*.

Table 7. Sample of H I detections – derived properties.

2MASX J (1)	l deg (2)	b deg (3)	A_K mag (4)	D Mpc (5)	$K_s^{o,d}$ mag (6)	$(J-K_s)^{o,d}$ mag (7)	$(H-K_s)^{o,d}$ mag (8)	$r_{K_s}^{o,d}$ kpc (9)	$\log(L_{K_c})$ $L_{\odot,K}$ (10)	$\log(M_{HI})$ $M_\odot$ (11)	$\log(\frac{M_{HI}}{L_{K_c}})$ $M_\odot/L_{\odot,K}$ (12)	V_{rot} km s^{-1} (13)	$\log(M_{dyn})$ $M_\odot$ (14)	$\log(\frac{M_{bar}}{M_{dyn}})$ (15)
00141253+7036448[v]	119.82	7.97	0.31	92.6	10.54	0.93	0.24	9.9	11.04	10.26	−0.78	277	11.25	−0.19
00384223+6017130	121.35	−2.55	0.22	55.0	10.67	0.89	0.21	5.7	10.54	9.43	−1.10	165	10.56	−0.06
0047543O+68074333[a,v]	122.60	5.26	0.35	50.0	10.37	0.92	0.33	7.7	10.57	9.80	−0.78	179	10.76	−0.17
0191829+6219297	126.16	−0.37	0.38	55.7	10.22	1.14	0.34	6.8	10.73	9.54	−1.19	151	10.55	0.12
0203021+6525055	125.95	2.72	0.40	54.3	9.47	0.88	0.26	9.2	11.01	9.87	−1.14	245	11.11	−0.15
0261932+6046064	127.18	−1.82	0.21	78.5	9.92	1.14	0.38	9.6	11.15	9.87	−1.27	298	11.30	−0.21
0273787+6308155	127.01	0.55	0.53	86.3	10.28	1.09	0.37	6.4	11.08	9.81	−1.28	83	10.01	1.01
01485859+6045514	129.90	−1.33	0.35	57.7	10.61	0.88	0.24	5.4	10.60	9.65	−0.95	145	10.42	0.16
01572719+6601408	129.58	4.01	0.41	53.9	10.08	1.66	0.52	4.5	10.75	9.25	−1.50	143	10.33	0.35
02013241+6824219[a,v]	129.34	6.41	0.35	48.3	9.19	0.89	0.25	8.9	11.02	9.08	−1.93	81	10.13	0.79

Columns 7 and 8: extinction-corrected colours $(H–K)^\circ$, $(J–K)^\circ$ determined within the r_{K20} isophotal radius (in mag). No additional size correction has been applied since isophotal colours are always measured at fixed aperture/radius.

Column 9: radius $r_{K_s}^{o,d}$ determined at the extinction-corrected SB level of 20 mag arcsec^{-2} in the K_s band (in kpc), hence corrected for the loss of the outer areas that lie below the 20th isophote due to extinction (see also Columns 6 and 7 in Table 5).

Column 10: extinction-corrected K_s-band luminosity L_{K_c}: within $r_{K20}^{o,d}$ (in L$_\odot$), for an assumed solar absolute magnitude of 3^m31 (Colina & Bohlin 1997) and the galaxy's distance D.

Column 11: total H I mass M_{HI}, where $M_{HI} = 2.356 \times 10^5 \cdot D^2 \cdot F_{HI}$ (in M$_\odot$).

Column 12: M_{HI}/L_{K_c}: ratio of the total H I mass to the extinction-corrected K_s-band luminosity (in solar units).

Column 13: V_{rot}: rotation speed corrected for inclination i; $v_{rot} = W_{50}/2\sin(i)$ for $\sin(i) < 0.2$, whereas for galaxies with higher inclinations we assumed $v_{rot} = W_{50}/2$ (in km s^{-1}).

*Column 14:* M_{dyn}: dynamical mass, estimated as $M_{dyn} = v_{rot}^2 \cdot r_{K20}^{o,d}/G$ (in M$_\odot$).

Column 15: M_{bar}/M_{dyn}: the ratio of the combined H I and stellar baryonic mass as a fraction of the total dynamical mass, where $M_{bar} = 0.8L_K + 1.4M_{HI}$ (McGaugh et al. 2000).

We now look at some of the global properties of the detected galaxies. Fig. 8 displays the H I mass versus recessional velocity. The coloured curves indicate the 3σ H I-mass detection limits for the NRT sensitivity limit of rms ~ 3 mJy and linewidths of $W_{50} = 150$ and 400 km s^{-1} respectively, the range that encompasses the majority of the detected galaxies. The figure reveals some clustering that coincides with the peaks in the velocity histogram (top panel of Fig. 7) and confirms that most of the detected galaxies hover around the PPS redshift of $cz \sim 6000$ km s^{-1}. At this distance, the H I masses of our detections lie between log M_{HI} of $9–10.5$M$_\odot$. Comparing this to the 3σ sensitivity curves indicates that we sample well below the characteristic log H I mass of 9.8 M$_\odot$ (Zwaan et al. 2005), marked in Fig. 8 as a dashed black line.

In Fig. 9 we present the H I mass, the extinction-corrected K_s-band luminosity $L_K^{d,o}$, and the dynamical mass M_{dyn}. The H I masses of the NRT detections range from $\log(M_{HI}) = 8.2–10.6$M$_\odot$ with the majority (80 per cent) confined to the narrow range of $9–10$M$_\odot$. The distribution is fairly symmetric around its mean (9.6 M$_\odot$). Its slightly offset maximum coincides closely with the characteristic H I mass, log $M_{HI}^* = 9.8$ M$_\odot$ derived by Zwaan et al. (2005) for the HIPASS survey (Meyer et al. 2004). The histogram confirms that we are not sensitive to low H I-mass galaxies, which are more prevalent in systematic H I surveys like HIZoA, HIPASS, and ALFALFA. Our detection rate is also a bit low on the high-mass range. The reason is that many of these will have been identified already in the shallower (rms ~ 6 mJy) 'blind' HIZoA.

The middle panel displays the respective luminosities of these same galaxies. The distribution is quite similar in shape as that of the H I masses, albeit shifted in log space by a value of $\Delta = 1.2$ to log$L_K = 10.8$ L$_\odot$, with a slightly lower dispersion. It reveals a similar tail towards lower values. The similarity of the log distributions is reflected in the average H I mass-to-light ratio which for this sample is $M_{HI}/L_K = -1.23$ M$_\odot$/L$_\odot$, in a narrow Gaussian distribution with a σ of 0.33 M$_\odot$/L$_\odot$.

The bottom panel presents the dynamical mass log (M_{dyn}). The peak as well as the mean of the distribution are close to that in the luminosity distribution, shifted only by $\Delta = 0.2$ towards higher luminosities in log space. The shape itself bears closer similarity to
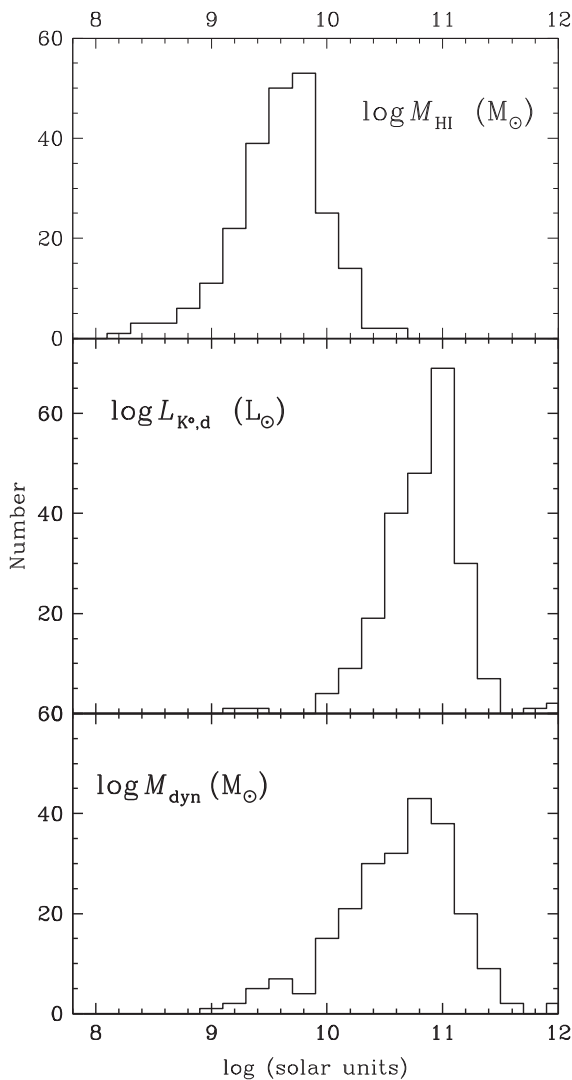
Figure 9. Global parameters of the certain and marginally detected galaxies, displayed as histograms. These are the logarithms of the HI-mass M_{HI}, the extinction-corrected K_s-band luminosity L_K, and the dynamical mass M_{dyn} (from top to bottom).

the HI-mass distribution, apart from the shift of 1.4. It is therefore not surprising that the ratio of the combined H I and stellar baryonic mass as a fraction of the total dynamical mass, is quite low on average, i.e. $M_{bar}/M_{dyn} = 0.17$, with a dispersion of $\sigma = 041$.

All these panels show a similar distribution to what was found – with much smaller numbers – for the NRT detections in our pilot project (van Driel et al. 2009).

6 UNVEILED LARGE-SCALE STRUCTURES

The description of the uncovered LSS revealed by the NRT detections is described below in context to known structures adjacent to the most obscured part of the Milky Way. Some preliminary results were given in Ramatsoku (2012) and Ramatsoku et al. (2014).

Fig. 10 displays in the top panel a histogram of the NRT detections as a function of Galactic longitude ℓ for the $\Delta\ell$-range visible from Nançay. The hashed part represents the new detections within $b < \pm5°$, while the open histogram includes all the NRT detections within $b < \pm10°$ (but not the higher latitude *EBV* sample). The

histogram identifies the newly unveiled filamentary ZoA crossings quite clearly. We have labelled the various peaks according to constellation (Puppis, Orion, Cassiopeia, Cygnus, and Ophiuchus) or features associated with known LSS (the PPS PP_I, the Supergalactic Plane SGP, and the second crossing that seems to form part of PPS crossing in Cygnus, dubbed PP_{II}). We will use this terminology henceforth for discussions of the structures. The highest peaks in the histogram are located within the previously hardly explored longitude range $70° < \ell < 180°$. As described in Section 1, this range is bounded by ZoA longitude strips accessible to Arecibo ($\ell \sim 180°-215°$ and $\ell \sim 70°-35°$), with some HI detections on either end of these strips from HIZoA and its northern extension ($\ell > 196°$, respectively $\ell < 52°$; Donley et al. 2005; Staveley-Smith et al. 2016).

The middle and bottom panels of Fig. 10 present the NRT detections in on-sky plots *merged* with redshifts available in the literature for 2MASX galaxies with the same magnitude limit ($K_s^o = 11^m25$). Hence, they constitute a low-latitude complement of the first 2MRS data release and the 2MTF survey. The galaxies are colour-coded in redshift shells of widths $\Delta V = 1500 \, km \, s^{-1}$, as a visual aid when tracing the continuity of structures in the redshift dimension. The galaxies below $2000 \, km \, s^{-1}$ were not plotted to not dilute the traced structures. Moreover, only five galaxies (2 per cent) were detected at these low redshifts. This is also true for the high-redshift range ($>8000 \, km \, s^{-1}$) where the scarcity of redshifts (4 per cent) due to survey sensitivity and RFI would not add much to the discussion.

The middle panel focuses on the 2MZOAG survey region ($|b| < 10°$). Here the NRT detections are outlined by squares. The bottom extends to latitudes of $|b| = 40°$ but without the squares to provide an unhampered view of how the ZoA structures link to the cosmic web beyond the ZoA. Note again the predominance of NRT detections in the $180° < \ell < 70°$ range: hardly any redshifts were known in the inner ZoA before the systematic 2MZOAG H I follow-up observations.

In the following. the new structures will be described in more detail. Note at the same time, the redshift slices out to $v_{hel} < 12\,000 \, km \, s^{-1}$ that are presented in Fig. 12 for the innermost ZoA ($|b| < 5°$, top panel) or the full range of the 2MZOAG survey ($|b| < 10°$, bottom panel). In the redshift wedges, red dots mark the new detections, while the blue crosses are 2MASX galaxies as listed in the 2MZOAG catalogue.

Puppis: the filamentary crossing around $\ell \sim 245°$ has first been explored by Kraan-Korteweg & Huchtmeier (1992). H I-follow-up observations of optically visible galaxies with the 100 m Effelsberg telescope uncovered various nearby groups at $v \sim 1500$ and $3000 \, km \, s^{-1}$. These have been corroborated by Staveley-Smith et al. (2016) with further indications of a condensation at $v \sim 7000 \, km \, s^{-1}$. The NRT results add further detections to these groupings, enhancing in particular the galaxy agglomeration around $7000 \, km \, s^{-1}$ (see also Fig. 12).

Orion: a notable peak in the histogram is found a bit further on around $\ell \sim 190°$ – located around the boundary of the Orion constellation (its top part) and Gemini (lower part), with a typical redshift around $v \sim 5000 \, km \, s^{-1}$. This crossing forms part of the extension of the so-called Gemini–Monoceros filament (Takata et al. 1994) which is weakly visible in the bottom panel of Fig. 12. It seems to extend from $(\ell, v) \sim (200°, 4000 \, km \, s^{-1})$ to $(190°, 6000 \, km \, s^{-1})$. The low velocity end of the Monoceros filament ($\ell \sim 210°$) discussed in the HIZoA surveys (Donley et al. 2005; Staveley-Smith et al. 2016) is, however, not as prominent in the 2MASX redshift distribution.
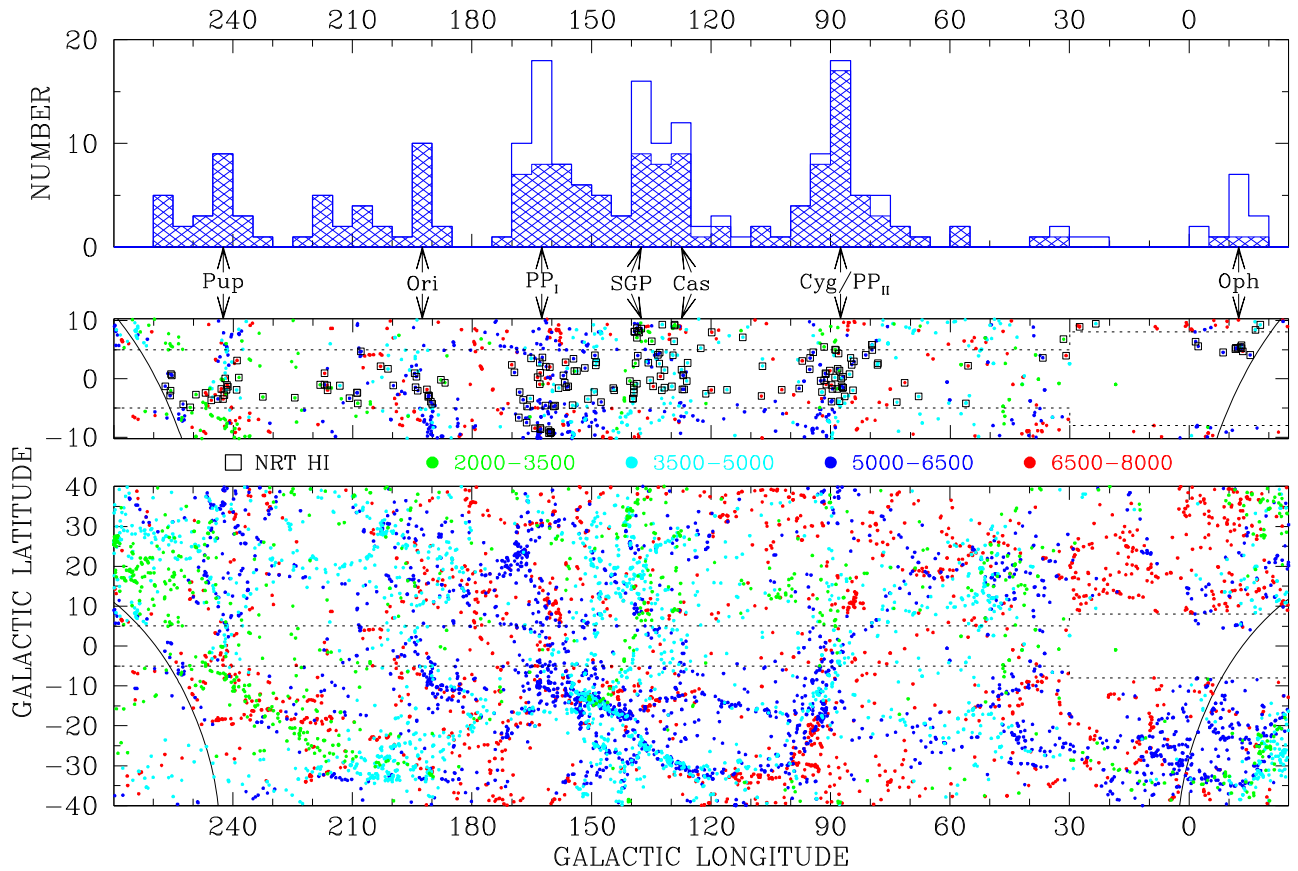
Figure 10. Top panel: histogram of the NRT HI detections within $|b| < 10°$ as a function of Galactic longitude, where hashed reflects the inner ZoA ($|b| < 5°$) with prominent peaks being labelled according to constellation. Bottom two panels: on-sky distribution in Galactic coordinates of the NRT-detected galaxies in the ZoA, together with 2MRS galaxies down to the same extinction-corrected NIR magnitude limit ($K_s^o \leq 11^m25$). Galaxies are displayed for the velocity range 2000–8000 km s^{-1} in which most (94 per cent) of the NRT detections reside. Colours indicate redshift intervals of 1500 km s^{-1} width. The middle panel displays the survey area with the new detections outlined by squares. The bottom panel displays a wider area for context of the large structures. The dashed lines mark the 2MRS exclusion zone ($|b| < 5°$; respectively $|b| < 8°$ for $0° \pm 30°$). The black lines mark the southern NRT declination limit.

The filament might further be connected to the N1600 supercluster (Saunders et al. 1991) at $(\ell, b, v) = (194°, +24°, 4400 \text{ km s}^{-1})$. Indeed, the bottom panel of Fig. 10 shows this filamentary crossing connecting to N1600 and back into the Plane around $\ell \sim 165°$ (discussed below) seems to be part of a circle surrounding a void centred at $\ell \sim 180°$. Given its velocity range (see the dominance of cyan and blue dots), it is not inconceivable that this structure is somehow interlinked with the PPS wall crossing.

Perseus−Pisces (PP$_I$) and its extension to Cygnus (PP$_{II}$):

The hidden cluster 3C 129: One of the highest peaks in the velocity histogram is centred around $\ell \sim 160°$. It looks less well-defined in the bottom panel of Fig. 10, but extends nearly vertically across the full width of the ZoA. The galaxies pertaining to this structure lie in the velocity range $v \sim 6000 \pm 1000$ km s^{-1}. Interestingly, two very strong radio galaxies are found along the path of this broad feature. Their position and redshifts ($v = 6236$ and 6655 km s^{-1}, respectively; Spinrad 1975) confirm that they reside inside the galaxy concentration. These are the head–tail radio source 3C 129 and the double-lobed giant elliptical radio galaxy 3C 129.1. The presence of radio sources with bent lobe morphology usually is indicative of a rich cluster environment. Indeed, hot X-ray emission surrounding these two radio galaxies was observed as part of the CIZA (X-ray Clusters in the ZoA) survey, i.e. CIZA J0450.0+4501 (Ebeling et al. 2000). The hot X-ray gas is centred on the radio galaxy 3C 129.1

which lies deep in the ZoA ($b = 0°27$). We do not see a prominent finger-of-god in Fig. 12 at the position of this cluster. In fact, hardly any NRT detections were made at the cluster core; this may well be caused by gas removal processes associated with the observed hot cluster gas of CIZA J0450.0+4501. In addition, NIR observations also suggested this cluster to be quite rich: despite being mostly invisible in the optical it stands out as a beacon in the photometric redshift sky distribution of the 'full' 2MASX catalogue (Jarrett 2004, e.g. Fig. 1).

To put this new cluster and wall crossing into context to the known structures adjacent to the ZoA, we list the most prominent clusters that define the quite distinct chain-like wall of the PPS (see cyan and blue dots below the Plane for the longitude range $\ell \sim 120°–160°$, in the bottom panel of Fig. 10, in order of *descending* latitude. In this list, we have already included Abell 569, which lies above the Galactic Plane, and the new ZoA link given by the cluster 3C 129 (or CIZA J0450.0+4501) at the Galactic equator. The clusters of the main PP complex then are:

Abell 569: $(\ell, b, v) \sim (168°, +23°, 6000 \text{ km s}^{-1})$
3C 129: $(\ell, b, v) \sim (160°, +.3°, 6300 \text{ km s}^{-1})$
LDCE 293[1]: $(\ell, b, v) \sim (162°, -10°, 6000 \text{ km s}^{-1})$
Perseus Cl: $(\ell, b, v) \sim (151°, -13°, 5400 \text{ km s}^{-1})$

---

[1]Crook et al. (2008) group catalogue based on the first 2MRS data release.
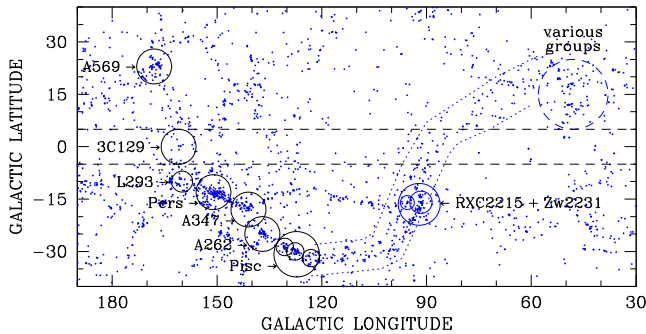
Figure 11. The PPS and its extensions across the ZoA. The figure is an extract of Fig. 10 limited to the PPS-velocity range (4500–7000 km s^{-1}). The various clusters and groups that form the primary chain (black circles) and its continuity and re-emergence into the ZoA are indicated (blue circles and dashed lines).

Abell 347: $(\ell, b, v) \sim (141°, -18°, 5500 \text{ km s}^{-1})$
Abell 262: $(\ell, b, v) \sim (137°, -25°, 5200 \text{ km s}^{-1})$
Pisces Cl: $(\ell, b, v) \sim (127°, -32°, 5400 \text{ km s}^{-1})$

Note that the Pisces Cloud really consist of a chain of three prominent galaxy groupings which from left to right are the NGC 507, NGC 383, and NGC 266 groups at the mean redshifts of 5700, 5200, and 4900 km s^{-1}, respectively.

For a better visualization of the PPS complex, we present with Fig. 11 an additional on-sky illustration. It is similar to the bottom panel of Fig. 10, but dedicated solely to the longitude and distance range which bears relevance to uncovered ZoA crossings PP$_I$ and PP$_{II}$) in Perseus and Cygnus. It is therefore restricted to the redshift range of 4500–7000 km s^{-1} and longitudes 30°–190°. The above listed clusters are identified in this plot as black circles with shortened labels corresponding to the above list, while the extension of the PP-chain towards Cygnus, and galaxy agglomerations embedded within it, are indicated with a blue trace.

The 3C 129 cluster and the wall in which it is embedded is located exactly in the extension between A 569 and the Perseus cluster (A 426). The herewith extended composition of the PP chain suggests the supercluster to be at least $\Delta\ell \sim 70°$ long at the mean distance of 5000–6000 km s^{-1}. The concept of a continuation of the PPS across the ZoA towards A569 in the northern Galactic hemisphere is not new. It was already hypothesized by Gregory, Thompson & Tifft (1981). Concerted efforts were made in the past to trace this prospective connection (Focardi, Marano & Vettolani 1984; Focardi et al. 1986; Chamaraux et al. 1990; Lu & Freudling 1995; Pantoja et al. 1997; Saurer, Seeberger & Weinberger 1997) through H I follow-up observations of optically identified galaxies. While the results were generally supportive of a connection, the data in this dust-enshrouded region were too sparse to be conclusive, partly because the hidden ZoA PP cluster discussed below remained inconspicuous.

Once the relevance of the optically hidden 3C 129 cluster as a new constituent of the PPS became apparent in the evolving NRT survey, a deep follow-up H I imaging survey project was launched with the Westerbork Synthesis Radio Telescope (WSRT) of a mosaic of 35 WSRT fields (9.6 sq deg), which includes the cluster and part of the wall in which it is embedded. Details can be found in Ramatsoku et al. (2016). Suffice to say that the cluster is confirmed as a rich cluster, showing evidence of H I deficiency at its core. Moreover, the main 3C 129 cluster seems to be undergoing a merger with a galaxy concentration that is in-falling along the PPS wall.
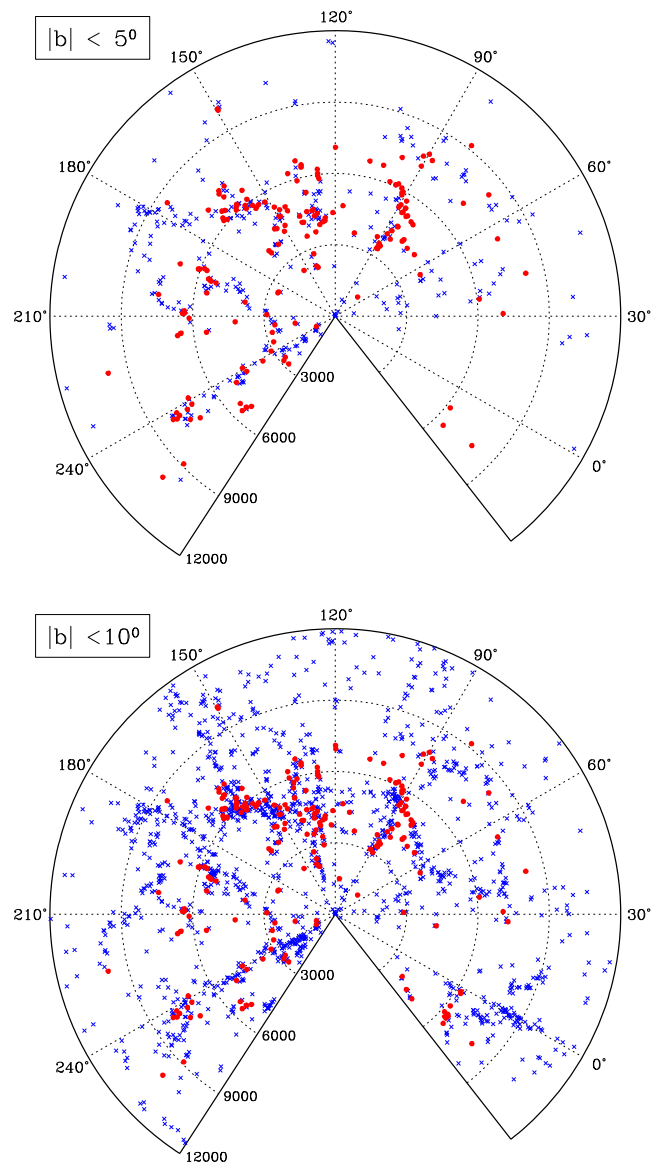
Figure 12. Redshift wedge out to $V_{hel} < 12\,000$ km s^{-1} centred on the longitude range of the Nançay 2MZOAG survey. Red dots represent NRT H I detections, and blue crosses 2MASX galaxies with prior redshift measurements. The top panel displays the inner ZoA ($|b| < 5°$) and the bottom panel the full width of the 2MZOAG survey ($|b| < 10°$). The most prominent new ZoA feature is the wall-like structure that forms part of the PPS (running from about $\ell \sim 125°$ at 4500 km s^{-1} to 165° and 6500 km s^{-1}). The latter includes the new filament around $\ell \sim 165°$ in which the 3C 129 cluster is embedded.

The Perseus-Pisces extension (PP$_{II}$) in Cygnus: the PPS chain does not abruptly end with the Pisces cluster: Fig. 11 shows that the chain seems to continue further on from the Pisces Cloud, albeit with a slightly less populated, thinner filament composed of an alignment of smallish groups, to about $(\ell, b) \sim (110°, -30°)$, marked by a blue dotted line, from where it bends upwards again towards the Galactic plane, traversing the X-ray cluster RXC J2215+3718 at $(\ell, b, v) \sim (92°, -16°, 5900 \text{ km s}^{-1})$ and the cluster ZwCl 2231.2+3732 $(95°, -18°, 6000 \text{ km s}^{-1})$ before re-entering the ZoA around $(\ell, b) \sim (90°, -10°)$. This is also evident in Fig 12. Most previous studies assumed the PPS stop and dissolve around this location, because no signature of a continuation on the other

side of the obscuring ZoA band was seen, not even in the dedicated optical ZoA galaxy searches by Seeberger et al. (1994). Our data clearly confirm continuity across the ZoA: on the northern side of the Galactic Plane (around $\ell \sim 80°$) the filament seems to continue with a shallower slope, towards an agglomeration of galaxy groupings centred around $(\ell, b) \sim (50°, +15°)$ (dashed blue circle in Fig. 11) at slightly lower velocities ($\sim$5000 km s^{-1}). This continuation across the plane is also visible in Fig. 12 as a wall-like structure within the $b < \pm 10°$ redshift slice; here we can trace the wall from $\ell \sim 80°$ at 6000 km s^{-1} to $\ell \sim 50°$ at 4500 km s^{-1}.

Fig. 11 implies the Perseus–Pisces chain to be considerably larger than evidenced in any previous survey of the PPS complex. Extending from the A569 cluster across the Plane, all the way back to where it re-enters the ZoA, resurfacing in the northern hemisphere around Cygnus, the feature spans a length of $\Delta \ell \sim 150°$ ($180°$ if we assume its continuation to $\ell \sim 50°$ to be real). This apparent contiguous band most likely has its origin in a cut through the surfaces of contiguous galaxy voids in the cosmic web of the nearby Universe, rather than one coherent structure of length of about $400h_{75}^{-1}$ Mpc. This would also explain the smooth increase and decrease in the average velocity of the PPS wall more readily.

SuperGalactic Plane and Cassiopeia: the concentration of detections between $\ell \sim 120°$–$140°$ seems – upon closer inspection – mostly due to two distinct features. This is also evident in the redshift shells based on the 2MASX photometric redshift plots (Jarrett 2004), as well as the 2MRS catalogue (Huchra et al. 2012) which exclude the inner ZoA. The thin filament around $\ell \sim 140°$ is nearer in velocity space (2500–3500 km s^{-1}) and forms part of the Supergalactic Plane. The agglomeration around $\ell \sim 130°$ is a bit broader, and at slightly higher velocities (around $v \sim 4500$ km s^{-1}), and seems less well defined. According to Fig. 10, it does link to the groupings around $(\ell, b) \sim (140°, +20°)$, whereas the redshift wedges (Fig. 12) suggest a wall-like structure that connects the Cas structure with the PPS ZoA wall discussed above, i.e. extending from $(\ell, v) \sim (120°, 4500$ km s$^{-1})$ to $(165°, 6500$ km s$^{-1})$, despite the low numbers of detections within the longitude range $120°$–$140°$.

Ophiuchus: following a fairly devoid stretch from about $\ell \sim 60°$ towards the GC – partly caused by the lack of 2MASS galaxies around the GC – a small peak appears in the histogram around $\ell = -10°$ ($\ell = 350°$). This is caused by galaxies in the $+5°$ to $+10°$ latitude strip. Fig. 12 suggest them to form part of the Ophiuchus supercluster (Wakamatsu et al. 1994, 2005) and the outer boundary of the Local Void.

7 CONCLUSIONS AND NEXT STEPS

As part of our long-term efforts to map the large-scale galaxy distribution and associated flow fields behind the Milky Way, we pursued a dedicated observing campaign with the 100 m class NRT to search for the H I emission and measure the redshifts of all bright NIR galaxies that so far had none.

Our NRT target list contained 1003 2MASS galaxies brighter than $K_s^o < 11^{\mathrm{m}}25$ across the ZoA ($|b| < 10°$) accessible from Nançay (Dec. $> -40°$). The majority of the galaxies without prior redshift measurement are located within the inner ZoA ($|b| < 5°$). They were selected from the newly defined 2MZOAG catalogue (Schröder, van Driel & Kraan-Korteweg, in preparation).

For the adopted sensitivity limit of rms = 3mJy and the redshift limit of $10\,600$ km s^{-1}, the 1800 h observing time allocated with the NRT led to the detection of 230 galaxies (of which 10 are marginal).

An additional 29 and 6 clear and marginal detections of non-target are presented.

The detection rate of the bright 2MZOAG sample was found to be independent of foreground extinction (Fig. 3), in agreement with what was found in the 'blind' HIZoA survey (Staveley-Smith et al. 2016). The 22 per cent detection rate is consistent with our pilot project (van Driel et al. 2009), and quite reasonable considering that no pre-selection on morphological type was made. Moreover, many of the brighter galaxies might have been targeted on earlier occasions.

The galaxies detected in this survey typically are H I-rich, with H I masses ranging in an interval of only $\log(M_{\mathrm{HI}}) = 8.2 - 10.6 \mathrm{M}_{\odot}$. However, only a handful of detections have masses below $9.0\,\mathrm{M}_{\odot}$. Given the NIR selection, it is not surprising that their stellar luminosities are fairly high: they hover with a narrow dispersion around a mean of $\log L_{\mathrm{K}} = 10.8$ (see Fig. 9), resulting in a small range in H I mass-to-light ratios as well.

The main goal of the Nançay observations presented here was the unveiling of the large-scale distribution of galaxies in the hitherto unexplored inner ZoA, particularly the northern ZoA in between the Arecibo strips ($70° < \ell < 180°$) for which hardly any recession velocities existed before (see Figs 9–11):

– the new Nançay detections add to our insight into the complex PPS structure. They confirm a continuation of the PPS from the Perseus cluster across the ZoA at $\ell \sim 160°$, connecting it to A 569 via the 3C 129 cluster (see Ramatsoku et al. 2016 for WSRT follow-up results of this cluster)

– a further extension shows the PPS to extend further than the Pisces clusters. It can be traced along a number of groups and clusters (see Figs 9 and 10), folding back into the ZoA in Cygnus ($\ell \sim 90°$) from where it seems to continue to the northern Galactic hemisphere. As such the PPS spans a length of about $150°$ ($\sim 400\,h_{75}^{-1}$ Mpc) on the sky

– two further filaments crossing the ZoA were identified in Cassiopeia ($\ell \sim 130°$) of which one forms part the SGP, with the other being a new feature at a slightly higher distance

– a sprinkling of detections in Ophiuchus (around the Galactic Bulge) appear to form part of the outer boundary of the LG, demonstrating the success of this project.

The results confirm this as a promising avenue to explore the ZoA, because neither the NIR photometry nor the H I radio emission are heavily affected by dust obscuration and stellar confusion. The combination of these data sets will in future allow the derivation of peculiar velocities through the NIR TF relation (see e.g. Said et al. 2015), and therewith a better understanding of the local dynamics, the cosmic flow fields and the underlying density field.

Our parallel projects with the goal of filling the 2MRS- and 2MTF-ZoA are also well underway. Further optical spectroscopic surveys of the 2MZOAG objects that have bright bulges, but were not detected in H I, have been launched. We have nearly completed the H I coverage of 2MASX ZoA galaxies for which only optical redshifts or low-quality H I profiles existed, and observed the more southern 2MZOAG with Parkes. And our complimentary approach of obtaining deep follow-up NIR imaging of galaxies detected in 'blind' H I surveys (e.g Staveley-Smith et al. 2016) has been completed. This inverse method is particularly successful around the Galactic Bulge, where 2MASX is incomplete.

The above projects can furthermore be regarded as precursors to the forthcoming SKA Pathfinder H I surveys, like WALLABY (Koribalski 2012; Duffy et al. 2012) with ASKAP (Johnston et al. 2008), APERTIF (Oosterloo, Verheijen & van Cappellen 2010) at Westerbork, and MeerKAT (Kraan-Korteweg et al. 2016), that will

all start within the next year and cover major parts of the ZoA to unprecedented depth and resolution.

ACKNOWLEDGEMENTS

REFERENCES

Beckmann V. et al., 2009, A&A, 505, 417

Butcher Z., Schneider S., van Driel W., Lehnert M. D., Minchin R., 2016, A&A, 596, A60

Carrick J., Turnbull S. J., Lavaux G., Hudson M. J., 2015, MNRAS, 450, 317

Chamaraux P., Cayatte V., Balkowski C., Fontanelli P., 1990, A&A, 229, 340

Chamaraux P., Masnou J.-L., Kazés I., Saitō M., Takata T., Yamada T., 1999, MNRAS, 307, 236

Colina L., Bohlin R., 1997, AJ, 113, 1138

Courtois H. M., Tully R. B., Fisher J. R., Bonhomme N., Zavodny M., Barnes A., 2009, AJ, 138, 1938

Crook A. C., Huchra J. P., Martimbeau N., Masters K. L., Jarrett T., Macri L. M., 2008, ApJ, 685, 1320

Djorgovski S., Thompson D. J., de Carvalho R. R., Mould J. R., 1990, AJ, 100, 599

Donley J. L. et al., 2005, AJ, 129, 220

Doyle M. T. et al., 2005, MNRAS, 361, 34

Dressler A., 1991, ApJS, 75, 241

Dressler A., Lynden-Bell D., Burstein D., Davies R. L., Faber S. M., Terlevich R., Wegner G., 1987, ApJ, 313, 42

Duffy A. R., Meyer M. J., Staveley-Smith L., Bernyk M., Croton D. J., Koribalski B. S., Gerstmann D., Westerlund S., 2012, MNRAS, 426, 3385

Ebeling H., Edge A. C., Allen S. W., Crawford C. S., Fabian A. C., Huchra J. P., 2000, MNRAS, 318, 333

Erdoğdu P. et al., 2006, MNRAS, 368, 1515

Fisher K. B., Huchra J. P., Strauss M. A., Davis M., Yahil A., Schlegel D., 1995, ApJS, 100, 69

Fitzpatrick E. L., 1999, PASP, 111, 63

Fixsen D. J., Cheng E. S., Gales J. M., Mather J. C., Shafer R. A., Wright E. L., 1996, ApJ, 473, 576

Focardi P., Marano B., Vettolani G., 1984, A&A, 136, 178

Focardi P., Marano B., Vettolani G., 1986, A&A, 161, 217

Giovanelli R., Haynes M. P., 1982, AJ, 87, 1355

Goncalves T. S., Martin D. C., Halpern J. P., Eracleous M., Pavlov G. G., 2008, Astron. Telegram, 1623

Gregory S. A., Thompson L. A., Tifft W. G., 1981, ApJ, 243, 411

Hauschildt M., 1987, A&A, 184, 43

Haynes M. P., Magri C., Giovanelli R., Starosta B. M., 1988, AJ, 95, 607

Haynes M. P. et al., 2011, AJ, 142, 170

Henning P. A., 1992, ApJS, 78, 365

Henning P. A., 1997, Publ. Astron. Soc. Aust., 14, 21

Henning P. A. et al., 2000, AJ, 119, 2686

Henning P. A. et al., 2008, in Minchin R., Momjian E., eds, AIP Conf. Ser., Vol. 1035, The Evolution of Galaxies Through the Neutral Hydrogen Window, Am. Inst. Phys., New York, p. 246

Henning P. A. et al., 2010, AJ, 139, 2130

Hewitt A., Burbidge G., 1991, ApJS, 75, 297

Hoffman Y., Courtois H. M., Tully R. B., 2015, MNRAS, 449, 4494

Hong T. et al., 2013, MNRAS, 432, 1178

Hong T. et al., 2014, MNRAS, 445, 402

Howlett C. et al., 2017, MNRAS, 471, 3135

Huchra J. P., Geller M. J., Corwin H. G., Jr, 1995, ApJS, 99, 391

Huchra J. et al., 2005, in Fairall A. P., Woudt P. A., eds, ASP Conf. Ser., Vol. 329, Nearby Large-Scale Structures and the Zone of Avoidance, Astron. Soc. Pac., San Francisco, p. 135

Huchra J. P., Macri L. M., Masters K. L., Jarrett T. H., Berlind P., Calkins M., 2012, ApJS, 199, 26

Huchtmeier W. K., Richter O. G., 1986, A&AS, 63, 323

Hudson M. J., Smith R. J., Lucey J. R., Branchini E., 2004, MNRAS, 352, 61

Jarrett T. H., 2004, Publ. Astron. Soc. Aust., 21, 396

Jarrett T. H., Chester T., Cutri R., Schneider S., Skrutskie M., Huchra J. P., 2000, AJ, 119, 2498

Jarrett T. H., Chester T., Cutri R., Schneider S. E., Huchra J. P., 2003, AJ, 125, 525

Johnston S. et al., 2008, Exp. Astron., 22, 151

Jones D. H., Read M. A., Saunders W., Colless M., Jarrett T., 2009, MNRAS, 399, 683

Kerp J., Winkel B., Ben Bekhti N., Flöer L., Kalberla P. M. W., 2011, Astron. Nachr., 332, 637

Kerr F. J., Henning P. A., 1987, ApJ, 320, L99

Kocevski D. D., Ebeling H., 2006, ApJ, 645, 1043

Koribalski B. S., 2012, PASA, 29, 359

Koribalski B. S. et al., 2004, AJ, 128, 16

Koss M., Mushotzky R., Veilleux S., Winter L. M., Baumgartner W., Tueller J., Gehrels N., Valencic L., 2011, ApJ, 739, 57

Kraan-Korteweg R. C., 2005, Rev. Mod. Astron., 18, 48

Kraan-Korteweg R. C., Huchtmeier W. K., 1992, A&A, 266, 150

Kraan-Korteweg R. C., Lahav O., 2000, A&AR, 10, 211

Kraan-Korteweg R. C., Woudt P. A., Cayatte V., Fairall A. P., Balkowski C., Henning P. A., 1996, Nature, 379, 519

Kraan-Korteweg R. C., Henning P. A., Schröder A. C., 2002, A&A, 391, 887

Kraan-Korteweg R. C., Shafi N., Koribalski B. S., Staveley-Smith L., Buckland P., Henning P. A., Fairall A. P., 2008, Astrophys. Space Sci. Proc., 5, 13

Kraan-Korteweg R. C., Jarrett T. H., Elagali A., Cluver M. E., Bilicki M., Colless M. M., 2015, in Buckley, D., Schröder, A.C., eds., SALT Science Conference 2015 (Proc. of Science: SSC2015), Stellenbosch Institute of Advanced Study, South Africa, p. 40

Kraan-Korteweg R. C. et al., 2016, in Taylor, R. Camilo, F., Leeuw, L. Moodley, K., MeerKAT, eds., On the Pathway to the SKA. (Proc. of Science: MeerKAT2016), Science: On the Pathway to the SKA, Proceedings of Science (MeerKAT2016), p. 21

Kraan-Korteweg R. C., Cluver M. E., Bilicki M., Jarrett T. H., Colless M., Elagali A., Böhringer H., Chon G., 2017, MNRAS, 466, L29

Lang R. H. et al., 2003, MNRAS , 342, L738

Lawrence A. et al., 1999, MNRAS, 308, 897

Loeb A., Narayan R., 2008, MNRAS, 386, 2221

Lu N. Y., Freudling W., 1995, ApJ, 449, 527

Lu N. Y., Dow M. W., Houck J. R., Salpeter E. E., Lewis B. M., 1990, ApJ, 357, 388

Martin J. M., Bottinelli L., Dennefeld M., Fouque P., Gouguenheim L., Paturel G., 1990, A&A, 235, 41

Martin A. M., Papastergis E., Giovanelli R., Haynes M. P., Springob C. M., Stierwalt S., 2010, ApJ, 723, 1359

Marzke R. O., Huchra J. P., Geller M. J., 1996, AJ, 112, 1803

Masters K. L., Springob C. M., Huchra J. P., 2008, AJ, 135, 1738

Masters K. L., Crook A., Hong T., Jarrett T. H., Koribalski B. S., Macri L., Springob C. M., Staveley-Smith L., 2014, MNRAS, 443, 1044

Matthews L. D., van Driel W., 2000, A&AS, 143, 421

McGaugh S. S., Schombert J. M., Bothun G. D., de Blok W. J. G., 2000, ApJ, 533, L99

Meyer M. J. et al., 2004, MNRAS, 350, 1195

Minchin R. F., et al., 2010, AJ, 140, 1093

Monnier Ragaigne D., van Driel W., Schneider S. E., Balkowski C., Jarrett T. H., 2003, A&A, 408, 465

Motch C. et al., 1998, A&AS, 132, 341

Nakanishi K., Takata T., Yamada T., Takeuchi T. T., Shiroya R., Miyazawa M., Watanabe S., Saito M., 1997, ApJS, 112, 245

O'Neil K., 2004, AJ, 128, 2080

Oosterloo T., Verheijen M., van Cappellen W., 2010, in van Leeuwen J., ed., ISKAF2010 Science Meeting, International SKA Forum, Proceedings of Science (ISKAF2010), p. 43

Pantoja C. A., Altschuler D. R., Giovanardi C., Giovanelli R., 1997, AJ, 113, 905

Parisi P., Masetti N., Jiménez-Bailón E., Chavushyan V., Malizia A., 2009, A&A, 507, 1345

Paturel G., Theureau G., Bottinelli L., Gouguenheim L., Coudreau-Durand N., Hallet N., Petit C., 2003, A&A, 412, 57

Radburn-Smith D. J., Lucey J. R., Woudt P. A., Kraan-Korteweg R. C., Watson F. G., 2006, MNRAS, 369, 1131

Ramatsoku M., 2012, Masters thesis, University of Cape Town

Ramatsoku M., Kraan-Korteweg R., Schröder A., van Driel W., 2014, in J.J. van Rensburg, ed., Proceedings of SAIP2012, p. 398

Ramatsoku M. et al., 2016, MNRAS, 460, 923

Riad I. F., 2010, PhD thesis, University of Cape Town

Riad I. F., Kraan-Korteweg R. C., Woudt P. A., 2010, MNRAS, 401, 924

Ricci C., Walter R., Courvoisier T. J.-L., Paltani S., 2011, A&A, 532, A102

Rosenberg J. L., Schneider S. E., 2000, ApJS, 130, 177

Ryan-Weber E., Koribalski B. S., Staveley-Smith L., Jerjen H., Kraan-Korteweg R. C., Ryder S. D., 2002, AJ, 124, 1954

Said K., Kraan-Korteweg R. C., Jarrett T. H., 2015, MNRAS, 447, 1618

Said K., Kraan-Korteweg R. C., Jarrett T. H., Staveley-Smith L., Williams W. L., 2016a, MNRAS, 462, 3386

Saintonge A., 2007, AJ, 133, 2087

Said K., Kraan-Korteweg R. C., Staveley-Smith L., Williams W. L., Jarrett T. H., Springob C. M., 2016b, MNRAS, 457, 2366

Saunders W. et al., 1991, Nature, 349, 32

Saunders W. et al., 2000, MNRAS, 317, 55

Saurer W., Seeberger R., Weinberger R., 1997, A&AS, 126, 247

Schlafly E. F., Finkbeiner D. P., 2011, ApJ, 737, 103

Schlegel D. J., Finkbeiner D. P., Davis M., 1998, ApJ, 500, 525

Schneider S. E., Helou G., Salpeter E. E., Terzian Y., 1986, AJ, 92, 742

Schneider S. E., Thuan T. X., Magri C., Wadiak J. E., 1990, ApJS, 72, 245

Schröder A. C., Kraan-Korteweg R. C., Henning P. A., 2009, A&A, 505, 1049

Scrimgeour M. I. et al., 2016, MNRAS, 455, 386

Seeberger R., Saurer W., 1998, A&As, 127, 101

Seeberger R., Huchtmeier W. K., Weinberger R., 1994, A&A, 286, 17

Skrutskie M. F. et al., 2006, AJ, 131, 1163

Spinrad H., 1975, ApJ, 199, L1

Spinrad H., Marr J., Aguilar L., Djorgovski S., 1985, PASP, 97, 932

Springob C. M., Haynes M. P., Giovanelli R., Kent B. R., 2005, ApJS, 160, 149

Springob C. M. et al., 2014, MNRAS, 445, 2677

Springob C. M. et al., 2016, MNRAS, 456, 1886

Staveley-Smith L., Kraan-Korteweg R. C., Schröder A. C., Henning P. A., Koribalski B. S., Stewart I. M., Heald G., 2016, AJ, 151, 52

Takata T., Yamada T., Saito M., Chamaraux P., Kazes I., 1994, A&AS, 104, 529

Strauss M. A., Huchra J. P., Davis M., Yahil A., Fisher K. B., Tonry J., 1992, ApJS, 83, 29

Tempel E., Stoica R. S., Martínez V. J., Liivamägi L. J., Castellan G., Saar E., 2014, MNRAS, 438, 3465

Tully R. B., Shaya K. J., Karachentsev I. D., Courtois H. M., Kocevski D. D., Rizzi L., Peel A., 2008, ApJ, 676, 184

van Driel W., Schneider S. E., Kraan-Korteweg R. C., Monnier Ragaigne D., 2009, A&A, 505, 29

van Driel W. et al., 2016, A&A, 595, A118

Visvanathan N., Yamada T., 1996, ApJS, 107, 521

Wakamatsu K., Hasegawa T., Karoji H., Sekiguchi K., Menzies J. W., Malkan M., 1994, in Balkowski C., Kraan-Korteweg R. C., eds, ASP Conf. Ser., Vol. 67, Unveiling Large-Scale Structures Behind the Milky Way, Astron. Soc. Pac., San Francisco, p. 131

Wakamatsu K., Malkan M. A., Nishida M. T., Parker Q. A., Saunders W., Watson F. G., 2005, in Fairall A. P., Woudt P. A., eds, ASP Conf. Ser., Vol. 329, Nearby Large-Scale Structures and the Zone of Avoidance, Astron. Soc. Pac., San Francisco, p. 189

Wilson T. L., Rohlfs K., Huttemeister S., 2009, Tools of Radio Astronomy. Springer-Verlag, Berlin

Wong O. I. et al., 2006, MNRAS, 371, 1855

Woudt P. A., Kraan-Korteweg R. C., Lucey J., Fairall A. P., Moore S. A. W., 2008, MNRAS, 383, 445

Yamada T., Takata T., Djamaluddin T., Tomita A., Aoki K., Takeda A., Saito M., 1993, ApJS, 89, 57

Yamada T., Tomita A., Saito M., Chamaraux P., Kazes I., 1994, MNRAS, 270, 93

Zwaan M. A. et al., 2003, AJ, 125, 2842

Zwaan M. A., Meyer M. J., Staveley-Smith L., Webster R. L., 2005, MNRAS, 359, L30

SUPPORTING INFORMATION

Supplementary data are available at *MNRAS* online.

Appendix A:. Notes to individual galaxies.

Please note: Oxford University Press is not responsible for the content or functionality of any supporting materials supplied by the authors. Any queries (other than missing material) should be directed to the corresponding author for the article.

This paper has been typeset from a TEX/LATEX file prepared by the author.